

# **Frequency Domain Beamforming in Acoustical Radiation Force Impulse Imaging**

By

Sai Prakash Reddy Konda

M.S., Wayne State University, Detroit, MI-USA, 2016.

B. Tech., Jawaharlal Nehru Technological University, Hyderabad, India, 2014.

A Report Submitted in Partial Fulfillment of the Requirements for the Degree of

MASTER OF ENGINEERING

In the Department of Electrical and Computer Engineering

Sai Prakash Reddy Konda, 2020

University of Victoria

All rights reserved. This report may not be reproduced in whole or in part, by photocopying or other means, without the permission of the author.

# Frequency Domain Beamforming in Acoustical Radiation Force Impulse Imaging

By

Sai Prakash Reddy Konda

M.S., Wayne State University, Detroit, MI-USA, 2016.

B. Tech., Jawaharlal Nehru Technological University, Hyderabad, India, 2014.

## Supervisory Committee

---

Dr. Daler Rakhmatov, **Supervisor**

(Department of Electrical and Computer Engineering)

---

Dr. Pan Agathoklis, **Departmental Member**

(Department of Electrical and Computer Engineering)

# ABSTRACT

## Supervisory Committee

---

Dr. Daler Rakhmatov, **Supervisor**

(Department of Electrical and Computer Engineering)

---

Dr. Pan Agathoklis, **Departmental Member**

(Department of Electrical and Computer Engineering)

---

Acoustical radiation force impulse (ARFI) imaging involves inducing and monitoring a tissue deformation response using an ultrasound transducer. At some location of interest, a typical ARFI sequence consists of three pulse types: 1) a reference pulse, used to establish a baseline position of the tissue before the excitation; 2) a pushing pulse, used to generate an acoustical radiation force to induce localized deformation; and 3) tracking pulses, applied immediately following the pushing pulse and used to monitor the tissue displacements over time. Applying such sequences of reference, pushing and tracking pulses can be used to generate 2D elastograms, i.e., images that characterize tissue stiffness, obtained by post-processing of the beamformed ARFI data.

In this work, we focus on the beamforming step, where we replace the conventional Delay-and-Sum (DAS) beamformer with a faster alternative called Frequency-Domain Migration (FDM). We also consider the low-cost data acquisition scenario (prior to beamforming), where the raw ARFI data is sampled at  $1/2$  rate, which is then followed by data interpolation using the Discrete Cosine Transform (DCT) to obtain the full-sized input expected by the FDM method. We use the above mentioned three methods (DAS, FDM, and DCT+FDM) to obtain the three versions of their respective beamformed ARFI data, each giving rise to the corresponding B-mode, displacement, and

elastographic images. To generate the latter, we have utilized the time-to-peak (TTP) estimation approach (based on linear regression) to determine shear-wave speed profiles of interest, followed by applying an averaging disc filter.

In our evaluations, we have used the public-domain experimental dataset that consists of four groups, or super frames (one per push), each containing 50 plane-wave tracking frames. Our results, based on ARFI imaging of a 10-mm 80-KPa sphere embedded in the 25-KPa background, show that the FDM and DCT+FDM methods are a viable alternative to the conventional and more expensive DAS method.

# Table of Contents

<b>Supervisory Committee</b> .....	<b>ii</b>
<b>Abstract</b> .....	<b>iii</b>
<b>Table of Contents</b> .....	<b>v</b>
<b>List of Tables</b> .....	<b>vii</b>
<b>List of Figures</b> .....	<b>viii</b>
<b>Acknowledgements</b> .....	<b>x</b>
<b>Dedication</b> .....	<b>xi</b>
<b>1 Introduction</b> .....	<b>1</b>
1.1 Various Imaging Methods .....	1
1.2 Report Scope and Contributions .....	4
<b>2 Background</b> .....	<b>5</b>
2.1 Acoustical Radiation Force Impulse (ARFI) Imaging .....	5
2.2 Generation of Acoustical Radiation Force (ARF) .....	6
2.3 Tissue Displacements .....	8
2.4 Monitoring Deformation Response .....	10
2.5 Structural Similarity Index Measurement (SSIM) .....	11
<b>3 Image Formation</b> .....	<b>13</b>
3.1 Delay-and-Sum (DAS) Beamforming .....	13
3.2 Frequency Domain Migration .....	15
3.3 Interpolation Using Discrete Cosine Transform (DCT) .....	16
3.3.1 Discrete Cosine Transform (DCT) .....	16
3.3.2 Interpolation via Zero Padding .....	17
<b>4 MATLAB Implementation</b> .....	<b>19</b>

4.1 Overview of USTB .....	19
4.2 Midprocess Implementation .....	20
4.3 DCT-Based Interpolation .....	22
4.4 Displacement Calculation .....	22
<b>5 Evaluation Results .....</b>	<b>24</b>
5.1 Description of ARFI Phantom .....	24
5.2 Imaging Results .....	25
5.3 Similarity of Displacement Images .....	37
5.4 Comparison of MATLAB Timing Profiles .....	38
<b>6 Elasticity Imaging .....</b>	<b>41</b>
6.1 Stiffness Quantification via Shear Wave Imaging .....	41
6.2 Elastographic Image Generation .....	43
6.3 Post-Filtering .....	50
<b>7 Conclusion and Future Work .....</b>	<b>56</b>
7.1 Conclusion .....	56
7.2 Future Work .....	57
<b>Bibliography .....</b>	<b>59</b>

# List of Tables

<b>Table No.</b>	<b>Table Name</b>	<b>Page No.</b>
5.1	Similarity of displacement images for DAS, FDM and DCT+FDM methods .....	38

# List of Figures

Figure Number	Figure Name	Page No.
1.1	Ultrasound-based elasticity imaging methods .....	2
1.2	General concept of ARFI-based elasticity imaging methods [52] .....	3
2.1	Simulated response in a 3D, homogeneous, isotropic, linear, elastic solid ( $E = 10$ KPa) depicting the axial displacements from an impulsive $45 \mu\text{s}$ , f-number 1.3, 6.7-MHz acoustic radiation force (ARF) excitation .....	9
2.2	Simulated response depicting the axial displacements from an impulsive $45 \mu\text{s}$ , f-number 1.3, 6.7-MHz acoustic radiation force excitation in a 3D linear, isotropic, elastic solid consisting of a stiffer material ( $E = 10$ KPa) centered between two softer materials ( $E = 2$ KPa) .....	10
3.1	DAS beamformer .....	14
4.1	Block diagram of ARFI data processing .....	20
4.2	Pseudo-code for FDM method .....	21
4.3	Pseudo-code for DCT+FDM method .....	22
5.1	(a). Top view of Spherical Phantom, highlighted is the imaged sphere, (b). Front view of Spherical Phantom, highlighted is the imaged sphere [51].....	24
5.2	B-Mode images for (a) DAS, (b) FDM and (c) DCT+FDM .....	26
5.3	Displacement images for (a) DAS, (b) FDM and (c) DCT+FDM: Frame 6 .....	28
5.4	Displacement images for (a) DAS, (b) FDM and (c) DCT+FDM: Frame 12 .....	29
5.5	Displacement images for (a) DAS, (b) FDM and (c) DCT+FDM: Frame 18 .....	31
5.6	Displacement images for (a) DAS, (b) FDM and (c) DCT+FDM: Frame 24 .....	32
5.7	Displacement images for (a) DAS, (b) FDM and (c) DCT+FDM: Frame 30 .....	34

5.8	Displacement images for (a) DAS, (b) FDM and (c) DCT+FDM: Frame 36 .....	35
5.9	Displacement images for (a) DAS, (b) FDM and (c) DCT+FDM: Frame 42 .....	37
5.10	MATLAB timing profiles for (a) DAS, (b) FDM and (c) DCT+FDM methods .....	39
6.1	Displacement time profile plotted for five chosen locations at various distances (2, 4, 6, 8, and 10 mm) away from the push .....	42
6.2	Linear regression results for our 5-point example .....	43
6.3	Images obtained by averaging across super frames, 13-pixel window size: (a) DAS, (b) FDM and (c) DCT+FDM methods .....	45
6.4	Images obtained by averaging across super frames, 20-pixel window size: (a) DAS, (b) FDM and (c) DCT+FDM methods .....	47
6.5	Images obtained by averaging across super frames, 27-pixel window size: (a) DAS, (b) FDM and (c) DCT+FDM methods .....	48
6.6	Images obtained by additional averaging across window sizes: (a) DAS, (b) FDM and (c) DCT+FDM methods .....	50
6.7	Filtered elastograms after applying 21-pixel disc averaging: (a) DAS, (b) FDM and (c) DCT+FDM methods .....	52
6.8	Filtered elastograms after applying 35-pixel disc averaging: (a) DAS, (b) FDM and (c) DCT+FDM methods .....	53
6.9	Filtered elastograms after applying 51-pixel disc averaging: (a) DAS, (b) FDM and (c) DCT+FDM methods .....	55

## **ACKNOWLEDGEMENTS**

Many thanks go to my supervisor, Dr. Daler Rakhmatov for providing his support academically and personally to the successful completion of this project. I would also like to acknowledge Dr. Pan Agathoklis for serving as a supervisory committee member.

I acknowledge my family who supported me all the way with their love and words of encouragement. My dad and mom, Mr. Ramesh Reddy Konda and Mrs. Prasanna Reddy Konda, you both were my backbone and rock throughout my academic journey. Thank you so much for all your prayers and encouragement.

## **DEDICATION**

This work is dedicated to my family and friends.

# Chapter 1

## Introduction

### 1.1 Various Imaging Methods

Ultrasound is commonly used to create images of internal body parts such as muscles, joints, tissues, etc. Plane wave (PW) ultrasound imaging is an important technique which allows for high frame rate image acquisition [20], [21], [53]. One of the important applications of PW ultrasound is acoustical radiation force (ARF) imaging [54]. The latter helps in characterizing the elastic properties of the tissues to capture pathological conditions when present. As opposed to conventional B-mode imaging that differentiates features with distinct acoustic properties, elasticity imaging methods differentiates features with distinct mechanical properties, and it requires both a forced excitation of soft tissues and monitoring of the deformation response. This response can be related to qualitative and/or quantitative measures of tissue stiffness.

The link between the elasticity of the tissues and their pathological conditions has been observed since early medicine. In 400 B.C., Hippocrates has noted that some abnormal swellings that are soft, free of pain, and yield when pressed with the finger, are more chronic compared with those that are painful, hard, and large, indicate danger of speedy death [1]. Manual palpation is commonly used in routine physical examinations to assess tissue health and monitor disease progression. For example, if there is a hard cyst found during routine breast exams, then it is often an early indication of breast cancer [2]-[7]. Although indispensable for medical diagnosis, manual palpation methods are relatively subjective and limited to superficial structures. With the ability to measure the elasticity of tissues deep within the body, ultrasound-based elasticity imaging techniques offer great clinical promise [6]-[8], [13], [15]-[18], [52], [53].

In 1990, Sugimoto *et al.* [54] proposed to produce the acoustical radiation force by ultrasound as a means of extending palpation methods to internal organs. Since then, a variety of ARF-based methods have been investigated. They are classified in Fig. 1.1 according to the temporal duration of the ARF excitation and the location of the tracking beams used to measure the deformation response. In general, the excitation (pushing) pulses can be applied: 1) quasi-statically to achieve a steady state response, 2) transiently in an impulse-like fashion, or 3) harmonically to excite the tissue at specific frequencies.

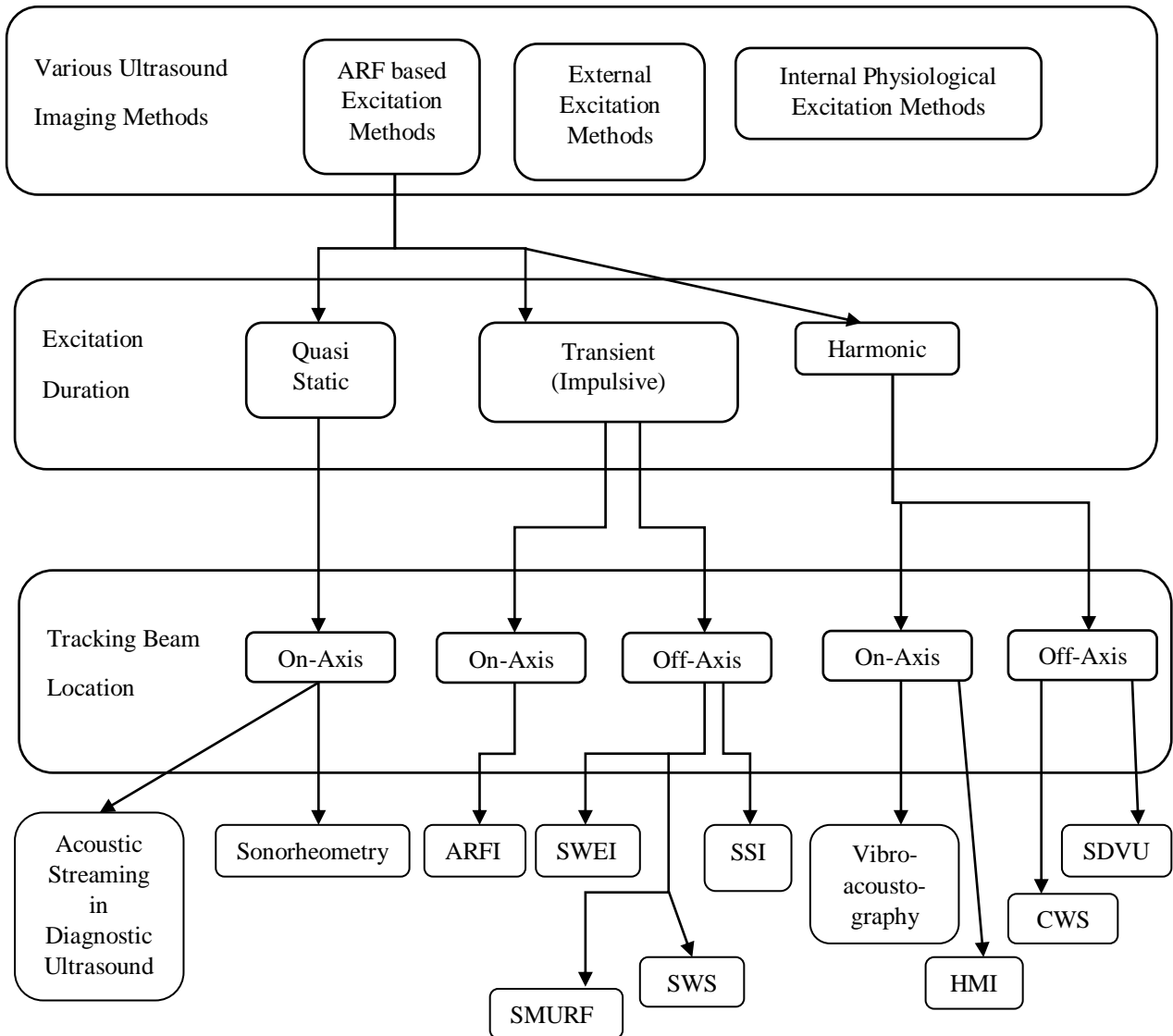


**Fig. 1.1.** Ultrasound-based elasticity imaging methods. **Source:** [52].

Among all these methods, we focus on acoustical radiation force impulse (ARFI) imaging.

This force is applied as an impulse at certain locations, which creates tissue displacement waves tracked using tracking pulses. These tracked pulses are compared with a previously applied reference pulse, in order to find the displacement estimates. Fig. 1.2 shows an example of an ARFI method that uses a focused transducer to generate a pulse causing a localized displacement. Using either a separate or the same remote device, the deformation can be monitored spatially and temporally. Since the force is applied directly on the region of interest, ARFI excitations possess smaller strains and are less impacted by external boundaries. Unlike other external excitation methods, they do not face problems associated with coupling the excitation within the targeted region.

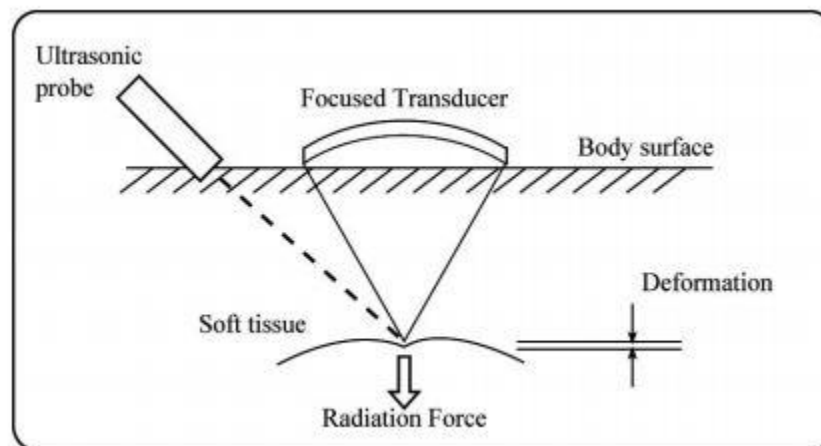


**Fig. 1.2.** General concept of ARFI-based elasticity imaging methods [52]. 1) A focused ultrasound transducer is used to generate sufficient acoustical radiation force (ARF) to cause localized tissue displacements. 2) The resulting deformation is monitored using the same or a separate remote device. **Source:** [52].

ARFI methods are advantageous in terms of ease of use, low cost, and lack of radiation. Moreover, a focused beam can be created by a tracking ultrasound probe itself to push the tissue. However, ARFI imaging has some disadvantages as well: it yields relatively low contrast between abnormal and surrounding tissues, it cannot be used for tissues located deep inside the body, and it is operator-dependent and subjective [52].

## 1.2 Report Scope and Contributions

As we have mentioned previously, this work is focused on ARFI imaging. Specifically, we consider an alternative image reconstruction process during PW-based deformation response tracking, whereby conventional Delay-and-Sum (DAS) beamforming of ARFI channel (raw) data is replaced by the recently proposed Frequency-Domain Migration (FDM) method [19]. Our motivation for using the latter is that it is computationally less expensive than the DAS method. Additionally, we also explore reducing the raw data acquisition cost by halving the temporal sampling rate. For example, if the full-rate data frame is of size  $N_t \times N_x$ , where  $N_t$  is the number of sampling time instances, and  $N_x$  is the number of sampled sensors in the transducer array, the half-rate data frame would be of size  $N_t/2 \times N_x$ , which means 50% savings in acquisition cost. Since the FDM method needs the full-sized raw data frame, we interpolate subsampled data using the Discrete Cosine Transform (DCT). Thus, this report also includes the assessment of the FDM method operating on the DCT-interpolated half-rate raw data input. We refer to this scheme of raw ARFI data processing as the DCT+FDM method.

We have used the MATLAB-based UltraSound ToolBox (USTB) framework to develop the code reported here. The original USTB package includes the reference implementations of DAS beamforming and displacement estimation methods, and we have used them without any modifications. We have added our implementations of the FDM and DCT+FDM methods (as an alternative to the DAS method), and we have also developed the displacement data processing code for generating elastographic images.

The rest of this report is organized as follows. Chapter 2 provides additional background on ARFI imaging. Chapter 3 details how the DAS, FDM, and DCT+FDM methods work. Chapter 4 outlines the USTB features and presents several pseudo-code snippets. Chapter 5 describes our experimental evaluation setup and presents both B-mode and displacement images obtained from three versions of the beamformed data, computed by the DAS, FDM, and DCT+FDM methods, respectively. Chapter 6 discusses how one can process the resulting displacement data further, to obtain useable elastographic images, which is the ultimate goal of ARFI imaging. Finally, Chapter 7 concludes this report and mentions possible directions for future work.

# Chapter 2

## Background

### 2.1 Acoustical Radiation Force Impulse (ARFI) Imaging

Acoustical Radiation Force Impulse (ARFI) imaging utilizes brief, high-energy acoustic pulses to excite the tissue response and ultrasonic correlation-based tracking to monitor the resulting displacement, which reflects the relative mechanical properties of tissue. ARFI imaging is useful for observing lesions that are difficult to visualize with conventional sonography, when the lesions are stiffer or softer than the surrounding tissue [2], [5], [6], [7], [17], [18], [46], [47], [52], [53], [56], [57]. ARFI imaging quality can be improved by using focused radiation force excitations at multiple axial and lateral locations throughout a 2D field of view [29], [32], [33], [38], [39], [46], [52], [53], [57].

ARFI imaging uses commercially available ultrasound scanners to generate short duration (approximately 30–300  $\mu\text{s}$ ) acoustic radiation forces. These impulses, or pushing pulses, generate localized tissue displacements of approximately 1–10  $\mu\text{m}$ . In general, the pushing frequency is at the lower end of the transducer bandwidth, while the transmit voltage is at the upper end of the system capability. The pushing pulses are similar to those used for Power Doppler imaging; however, they are much longer in duration (e.g., 200 cycles vs. 10 cycles). Radiation force that is sufficient to generate displacements in soft tissue on the order of tens of microns is typically achievable within standard diagnostic limits [46], [47], [48], [52].

The response of the tissue to the radiation force is observed using conventional B-mode imaging pulses to track tissue displacements. However, the depths at which these displacements can be generated are shallower than the corresponding maximum B-mode imaging depth for a given transducer. This is due to the attenuation of sound in the intervening tissue, and the fact

that more energy is required to push the tissue than to image it. To increase depth penetration while maintaining displacement resolution, the use of separate imaging arrays (higher frequency) and pushing arrays (low frequency) may be beneficial. This approach is under investigation in the application of monitoring High Intensity Focused Ultrasound (HIFU) thermal ablation procedures [58], [59]. Two- or three-dimensional images of tissue displacement can be created by repeating this process along multiple image lines.

## 2.2 Generation of Acoustical Radiation Force (ARF)

Several groups are investigating the use of elasticity imaging in ultrasound. These methods can be classified according to the source of excitation used to deform the tissue. The first ultrasound-based elasticity imaging methods depends upon the use of an external source, such as a transducer to compress the skin as in elastography, or strain imaging. Similarly, a mechanical vibrator can be used to vibrate the tissue at specific frequencies in sonoelasticity. Natural, physiological based sources can also be used to deform the tissue. These methods take advantage of breathing, cardiac motion, or arterial pulsation to derive elasticity information.

The deformation caused by the applied force is associated with a restoring stress that satisfies equilibrium and a strain describing the deformation. Newton's second law can be used to express in terms of stress as follows [52]:

$$f_i = \frac{\partial \sigma_{ij}}{\partial x_j} = \rho a_i, \quad (1)$$

where  $f$  is the applied force,  $a$  is the particle acceleration,  $\rho$  is the material density,  $\sigma$  is stress, and  $x$  is a spatial coordinate. The strain gives the information about the deformed configuration of a material to its initial reference, specifically representing the change in length per unit length. The strain  $\varepsilon$  can be expressed in terms of displacement  $u$  as follows [52]:

$$\varepsilon_{ij} = \frac{1}{2} \left( \frac{\partial u_i}{\partial x_j} + \frac{\partial u_j}{\partial x_i} + \frac{\partial u_j}{\partial x_i} \frac{\partial u_i}{\partial x_j} \right). \quad (2)$$

The elasticity of a material describes its tendency to deform in response to an applied force, and the goal of elasticity imaging methods is to relate stress and strain. In general, soft tissues are viscoelastic, inhomogeneous and anisotropic. As viscoelastic materials, soft tissues exhibit

properties of both elastic solids and viscous fluids, whose particular response is dependent upon the frequency of excitation. Ignoring viscous forces and neglecting the non-linear terms, soft tissues are often described to a first-order approximation as linear, elastic solids. If homogeneous and isotropic conditions are also assumed, a constitutive equation describing the relationship between stress and strain can be represented as [52]:

$$\sigma_{ij} = \lambda \varepsilon_{kk} \delta_{ij} + 2\mu \varepsilon_{ij}, \quad (3)$$

where  $\lambda$  and  $\mu$  are Lamé constants,  $\varepsilon_{kk}$  is the normal strain,  $\varepsilon_{ij}$  is the shear strain, and  $\delta$  is Kronecker delta.

In the ultrasound literature, the tissue stiffness is commonly reported in terms of the Young's modulus  $E$ , which describes a material's resistance to deformation in uniaxial compression or tension. The shear modulus  $\mu$  describes the resistance to shear. The Poisson's ratio  $\nu$  describes the deformation that occurs orthogonal to that of the applied force. For a homogeneous, isotropic, linear elastic material, these moduli completely define the elasticity of the material and are related according to [52]:

$$E = \frac{\mu(3\lambda+2\mu)}{\lambda+\mu}, \quad (4)$$

$$\nu = \frac{\lambda}{2(\lambda+\mu)}, \quad (5)$$

$$\mu = \frac{E}{2(1+\nu)}. \quad (6)$$

For all the incompressible materials, we have  $\nu = 0.5$  and  $\mu = E/3$  [52].

Acoustical radiation force (ARF) generation results from the transfer of momentum from an ultrasonic wave in an attenuating medium, where the pressure and particle velocity become out of phase. At ultrasonic frequencies, soft tissues do not support shear stresses and are more accurately modeled as viscous fluids. For an incompressible material, the equation for a linear viscous fluid can be described by [52]:

$$\sigma_{ij} = -p\delta_{ij} + \left(k - \frac{2}{3}\mu_f\right) D_{kk}\delta_{ij} + 2\mu_f D_{ij}, \quad (7)$$

where  $D$  represents the rate of deformation,  $p$  is a scalar pressure,  $k$  is bulk viscosity, and  $\mu_f$  is shear viscosity. On the other hand, the particle acceleration  $\bar{a}$  can be expressed as [52]:

$$\bar{\mathbf{a}} = \frac{\partial \tilde{\mathbf{v}}}{\partial t} + \tilde{\mathbf{v}} \cdot \nabla \tilde{\mathbf{v}}, \quad (8)$$

where  $\tilde{\mathbf{v}}$  represents the particle velocity, and  $\nabla$  is the spatial gradient operator. Combining Eq. (1) and (8) yields:

$$-\nabla p + \left(k + \frac{\mu_f}{3}\right) \nabla(\nabla \cdot \tilde{\mathbf{v}}) + \mu_f \nabla^2 \tilde{\mathbf{v}} = \rho \left(\frac{\partial \tilde{\mathbf{v}}}{\partial t} + \tilde{\mathbf{v}} \cdot \nabla \tilde{\mathbf{v}}\right). \quad (9)$$

The right-hand side of Eq. (9) can be approximated as follows [52]:

$$\rho_0 \frac{\partial \tilde{\mathbf{v}}_2}{\partial t} + \frac{\partial \rho_1 \tilde{\mathbf{v}}_1}{\partial t} + \rho_0 (\tilde{\mathbf{v}}_1 \nabla \cdot \tilde{\mathbf{v}}_1 + \tilde{\mathbf{v}}_1 \cdot \nabla \tilde{\mathbf{v}}_1), \quad (10)$$

where  $\rho_0$  represents the material density,  $\tilde{\mathbf{v}}_1$  and  $\rho_1$  are first-order approximations for the particle velocity and density, respectively, and  $\tilde{\mathbf{v}}_2$  is a higher-order correction term representing the acoustic streaming velocity. Taking the time-average of the above expression leads to the following equation for the acoustical radiation force  $F$  [52]:

$$F = \rho_0 \langle \tilde{\mathbf{v}}_1 \nabla \cdot \tilde{\mathbf{v}}_1 + \tilde{\mathbf{v}}_1 \cdot \nabla \tilde{\mathbf{v}}_1 \rangle. \quad (11)$$

For an exponentially attenuating plane wave, this force can be expressed in terms of the time-averaged intensity  $I$  at any given spatial location as follows [52]:

$$F = 2\alpha I / c_L, \quad (12)$$

where  $\alpha$  is the absorption coefficient, and  $c_L$  is the longitudinal wave speed. Peak magnitudes of  $F$  are typically on the order of dynes, causing tissue displacements in the order of 1-10  $\mu\text{m}$ .

## 2.3 Tissue Displacements

Fig. 2.1 illustrates the axial displacements induced in a 3D homogeneous, isotropic, linear, elastic solid model with  $E = 10$  KPa using a 45- $\mu\text{s}$  6.7-MHz impulse excitation with f-number 1.3. The (transmit) f-number refers to the ratio of the focal depth  $z$  to the aperture width  $D$ , i.e., f-number =  $z/D$ .

The response at three time steps following the application of the acoustical radiation force is portrayed in Figs. 2.1(a)-(c). Initially, the acoustical radiation force is localized within the focal zone, often referred to as the region-of-excitation (ROE), resulting in the peak displacement in Fig. 2.1(a). Shear waves created at the edges of the ROE propagate orthogonally to the direction

of the applied force, causing off-axis displacements of decreased magnitude resulting from a spreading of the acoustic energy depicted in Figs. 2.1(b) and 2.1(c). The response recorded through time at three locations, distributed across the lateral dimension within (pink cross) and outside (red circle and green square) the ROE, is depicted in Fig. 2.1(d).

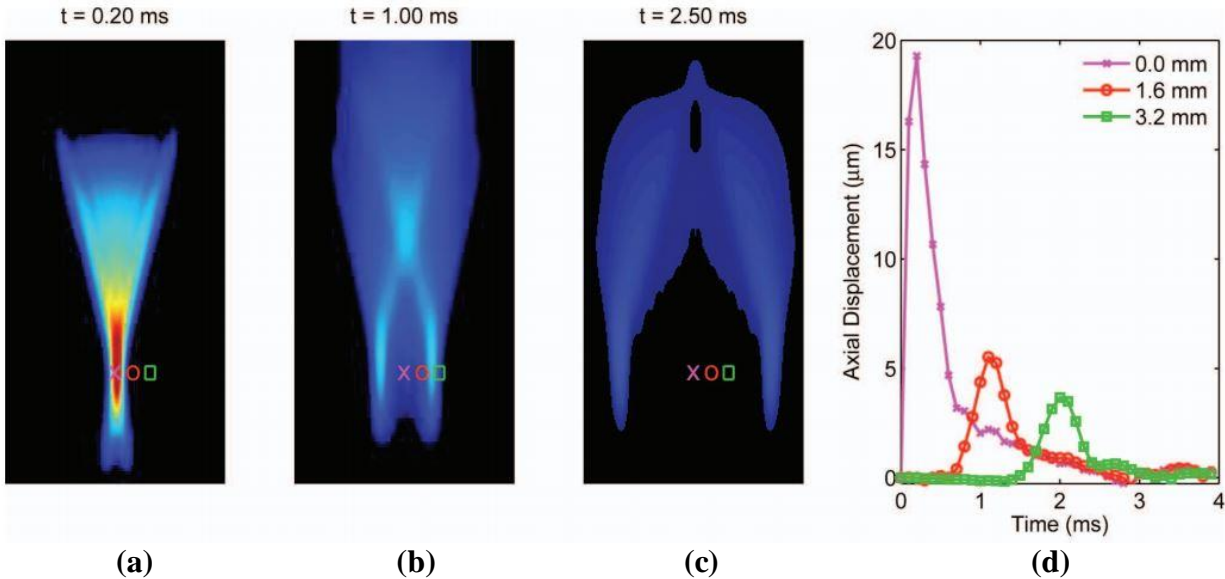


**Fig. 2.1.** Simulated response in a 3D, homogeneous, isotropic, linear, elastic solid ( $E = 10$  KPa) depicting the axial displacements from an impulsive  $45 \mu\text{s}$ , f-number 1.3, 6.7-MHz acoustic radiation force (ARF) excitation. The axial displacements depicted at 3 different time steps following excitation in (a) through (c) show the propagation of shear waves away from the region-of-excitation (ROE). (d) The displacement through-time profiles show the axial displacements occurring at the focal depth for each of 3 separate lateral locations, located both on-axis (pink cross) and off-axis (red circle and green square). These profiles reflect the decreased displacement amplitude with increased distance from the ROE caused by geometric spreading. **Source:** [52].

In heterogeneous soft tissues, this dynamic response becomes much more complicated because of wave reflections at material boundaries and acoustic impedance mismatches. With the white-dashed lines depicting the material boundaries between a 10-kPa central layer and two softer 2-kPa outer layers, Fig. 2.2 illustrates such a response for the same transducer configuration as in Fig. 2.1. In Fig. 2.2(d), note the presence of multiple distinct peaks indicative of the initial shear wave propagating away from the ROE, and also the reflected shear wave traveling back toward the ROE [52].

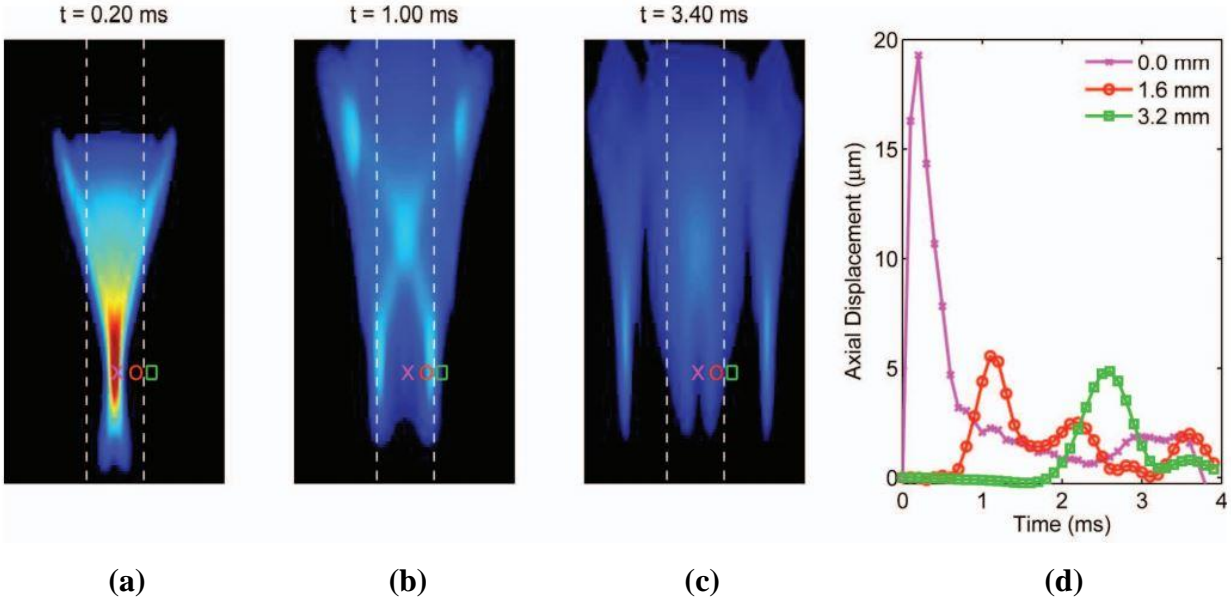


**Fig. 2.2.** Simulated response depicting the axial displacements from an impulsive  $45 \mu\text{s}$ ,  $f$ -number 1.3, 6.7-MHz acoustic radiation force excitation in a 3D linear, isotropic, elastic solid consisting of a stiffer material ( $E = 10$  KPa) centered between two softer materials ( $E = 2$  KPa). The material boundaries are indicated by the white dashed lines in (a) through (c), which depict the axial displacements at 3 distinct times following excitation. In (b) the shear waves have not reached the layer boundaries and only the initial shear waves propagating from the region-of-excitation (ROE) are observed. In (c), just after the shear waves reached the center material boundary, the reflected and transmitted waves are depicted. (d) The displacement-through-time profiles show multiple distinct peaks indicative of both the incident shear waves and the reflected shear waves introduced by the material boundaries. **Source:** [52].

## 2.4 Monitoring Deformation Response

ARFI imaging methods rely upon the ability to accurately monitor the tissue motion induced by the applied force. Using conventional pulse-echo ultrasound, the tissue motion can be monitored spatially and temporally. Tissue displacements can be estimated with cross-correlation or phase-shift-based algorithms, involving signals collected before the excitation (reference) and after the excitation (tracking).

Cross-correlation methods were originally developed for estimating blood flow velocities [52]. This technique, often referred to as time-delay estimation, measures the similarity between windowed data sections from the reference and tracking signals. The time shift that results in the

maximum cross-correlation value indicates when the two signals are most similar, which is then used to compute a displacement estimate. The normalized cross-correlation (NCC) method reduces the impact of bright scatterers and is often considered the gold standard for ultrasonic displacement estimation [52].

Alternatively, phase-shift methods allow for real-time 2D color flow imaging to be done using 1D autocorrelation estimation [42], [43]. Unlike cross-correlation methods that operate in the time domain, phase-shift methods operate in the frequency domain, typically utilizing demodulated in-phase and quadrature (IQ) data. Improved performance can be obtained using the 2D autocorrelation method, which accounts for local variations in the center frequency of the received echo for each displacement estimate [42], [43]. For the small displacements typically encountered with ARFI methods, the 2D autocorrelation method performs reasonably well compared with normalized cross correlation and is less computationally intensive. In chapter 4 we provide further details on how autocorrelation-based displacement estimates are computed in this work.

## 2.5 Structural Similarity Index Measurement (SSIM)

Given that we are evaluating different image formation methods in this work, we need to compare the resulting images quantitatively. One such numerical indicator is based on the so-called Structural Similarity Index Measurement (SSIM), introduced in [64] in order to quantify how similar two images  $I_1$  and  $I_2$  are. SSIM ranges from  $-1$  to  $+1$ , the latter indicating that the two images under consideration are identical.

The value of  $SSIM(I_1, I_2)$  is dependent on luminance factor  $l(I_1, I_2)$ , contrast  $c(I_1, I_2)$ , and structure  $s(I_1, I_2)$ , as defined below [64]:

$$SSIM(I_1, I_2) = [[l(I_1, I_2)^{p_1}] \cdot [c(I_1, I_2)^{p_2}] \cdot [s(I_1, I_2)^{p_3}]], \quad (13)$$

$$l(I_1, I_2) = \frac{2Mean_{I_1}Mean_{I_2}+c_1}{Mean_{I_1}^2+Mean_{I_2}^2+c_2}, \quad (14)$$

$$c(I_1, I_2) = \frac{2Var_{I_1}Var_{I_2}+c_1}{Var_{I_1}^2+Var_{I_2}^2+c_2}, \quad (15)$$

$$s(I_1, I_2) = (Var_{I_1I_2} + C_3) \frac{1}{Var_{I_1}Var_{I_2}+C_2}, \quad (16)$$

where  $Mean_{I_1}$ ,  $Mean_{I_2}$ ,  $Var_{I_1}$ ,  $Var_{I_2}$ , and  $Var_{I_1I_2}$  are local mean, variance, and cross-covariance values for the respective images. Constants  $C_1$ ,  $C_2$ ,  $C_3$  and exponential parameters  $p_1 > 0$ ,  $p_2 > 0$ ,  $p_3 > 0$  are used to adjust luminance, contrast, and structure. In our work, we are using default settings:  $p_1 = p_2 = 0$ ,  $p_3 = 1$ ,  $C_1 = C_2 = C_3 = 0$ .

# Chapter 3

## Image Formation

### 3.1 Delay-and-Sum (DAS) Beamforming

Fig. 3.1 presents the block diagram of a conventional Delay-and-Sum (DAS) beamformer. Time delays  $\tau_1, \tau_2, \tau_3, \dots, \tau_M$  are used to focus the signals  $p_1, p_2, p_3, \dots, p_M$  received from  $M$  equally spaced sensors. The delayed signal samples are denoted by  $q_1, q_2, q_3, \dots, q_M$ . Next, they are multiplied by their respective weighting coefficients  $w_1, w_2, w_3, \dots, w_M$ , and then summed to produce the final beamformed signal  $y$ . This process of applying weights to the input signals is called apodization. Such weights can be either adaptive or non-adaptive (fixed).

Adaptive beamforming can achieve a narrow main lobe with its side lobes suppressed, which improves image quality in terms of resolution, brightness, and contrast [60]. However, the adaptive weight vector must be continuously recalculated based on the received input signal characteristics. In case of non-adaptive beamforming, fixed window functions will determine the weight vector, which can be rectangular, Hamming, Hanning, Kaiser, Tukey, and others [60]. This type of beamforming is data independent, and an appropriate window function should be chosen carefully. In this work, we are using non-adaptive DAS beamforming with a rectangular window.

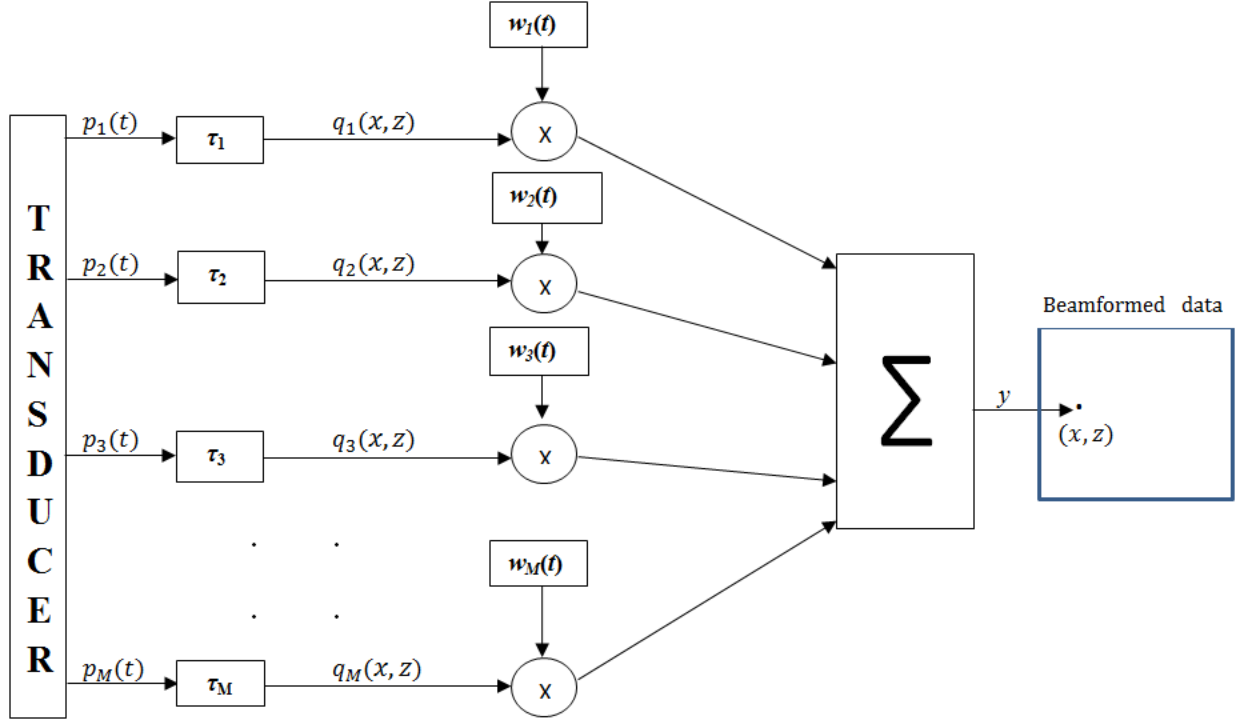


**Fig. 3.1.** DAS beamformer.

In plane-wave (PW) imaging, the said  $M$  sensors are used for both PW transmission and echo reception. For each plane wave  $e$ , emitted at angle  $\theta_e$ , and element  $m$  of the transducer array, the recorded signal over time  $t$  is represented by  $p_{m,e}(t)$ . Our goal is to obtain appropriately delayed data  $q_{m,e}(x, z)$ , where  $x$  is the lateral axis and  $z$  is the depth axis. Assuming the constant speed of sound  $c_s$  in the tissues (typically 1540 m/s) and spherical wavefronts due to backscatter, we have [60], [63]:

$$q_{m,e}(x, z) = p_{m,e}(\tau_{m,e}(x, z)), \quad (17)$$

where  $\tau_{m,e}(x, z)$  is the sum of the transmit delay  $\tau_{\text{TX},e}(x, z)$  and the receive delay  $\tau_{\text{RX},m}(x, z)$ , as specified below.

$$\tau_{m,e}(x, z) = \tau_{\text{TX},e}(x, z) + \tau_{\text{RX},m}(x, z), \quad (18)$$

$$\tau_{\text{TX},e}(x, z) = \frac{1}{c_s} [x \sin(\theta_e) + z \cos(\theta_e)], \quad (19)$$

$$\tau_{\text{RX},m}(x, z) = \frac{1}{c_s} \cdot \sqrt{(x - x_m)^2 + z^2}, \quad (20)$$

Note that  $x_m$  is a lateral position of the  $m^{\text{th}}$  element of the array. Thus [64],

$$q_{m,e}(x, z) = p_{m,e} \left( \frac{1}{c_s} \left\{ [x \sin(\theta_e) + z \cos(\theta_e)] + \sqrt{(x - x_m)^2 + z^2} \right\} \right). \quad (21)$$

Finally, we need to sum the  $q_{m,e}(x, z)$  values over all  $m$ , after multiplying them by  $w_m$ , which yields the desired beamformed output:

$$y_e(x, z) = \sum_m w_m q_{m,e}(x, z). \quad (22)$$

### 3.2 Frequency Domain Migration

PW ultrasound image formation can also be performed in the frequency domain. Firstly, the echoes recorded in the  $(x, t)$  domain undergo the 2D Fourier Transform to obtain the signals in the  $(k_x, f)$  domain. Here,  $x$  represents the spatial axis (i.e., the transducer element locations), and  $k_x$  denotes the spatial frequencies, while  $t$  denotes the time axis, and  $f$  denotes the temporal frequencies. Next,  $(k_x, f)$  data points are mapped into the  $(k_x, k_z)$  domain via spectral interpolation, where  $k_z$  denotes the spatial frequencies in relation to the  $z$ -axis (imaging depth). From this spectrum, the required 2D beamformed data in the  $(x, z)$  domain is obtained by performing the 2D Inverse Fourier Transform.

In this work, we use one of such methods that has been recently proposed in [19]. We shall refer to it as the Frequency Domain Migration (FDM) method. The motivation behind selecting this method is that its computational complexity is lower in comparison to DAS beamforming. The FDM method involves the following four steps.

**Step 1:** Let  $P_e(x, t)$  represent a scalar wave field recorded by the transducer at the surface (depth  $z = 0$ ) after emitting a plane wave at an angle  $\theta_e$ , and let  $\Psi_e(k_x, f)$  be the 2D frequency domain representation of  $P_e(x, t)$ :

$$\Psi_e(k_x, f) = \iint P_e(x, t) e^{-j2\pi(k_x x + ft)} dx dt. \quad (23)$$

**Step 2:** For each  $k_x$ , obtain  $\tilde{\Psi}_e(k_x, k_z)$  from  $\Psi_e(k_x, f)$  via interpolation along the  $f$ -axis and amplitude scaling as shown below. Set  $\tilde{\Psi}_e(k_x, k_z) \leftarrow 0$  whenever  $k_z^2 \leq k_x^2$ :

$$\tilde{\Psi}_e(k_x, k_z) = \frac{c_s \Psi_e(k_x, c_s k_z \sqrt{1 + (k_x/k_z)^2} / [1 + \cos \theta_e])}{[1 + \cos \theta_e] \sqrt{1 - (k_x/k_z)^2}}, \quad (24)$$

$$k_z = (f/c_s) \left[ 1 + \sqrt{1 - \left( \frac{c_s k_x}{f} \right)^2} \right], \quad f^2 > c_s^2 k_x^2. \quad (25)$$

**Step 3:** Apply the 1D Inverse Fourier Transform to  $\tilde{\Psi}_e(k_x, k_z)$  along the  $k_x$ -axis, and multiply the resulting spectrum  $\tilde{\Psi}_e(x, k_z)$  by  $e^{jnk_z x \tan \theta_e}$ .

**Step 4:** Apply the 1D Inverse Fourier Transform along the  $k_z$ -axis, which produces the desired beamformed output  $P_e(x, z)$ .

### 3.3 Interpolation Using Discrete Cosine Transform (DCT)

One way to reduce the amount of raw data recorded during PW-based displacement tracking is to lower the temporal sampling rate of the ultrasound transducer. For example, lowering the said rate by a factor of 2 reduces a raw data frame size from  $N_t \times N_x$  to  $N_t/2 \times N_x$ , which amounts to 50% sample savings.

In this chapter, we consider using the Discrete Cosine Transform (DCT) to recover raw data samples missing due to the temporal sampling rate reduction. Essentially, our aim is to apply DCT-based interpolation to resize a subsampled raw data frame to its fully sampled size, which can also be viewed as “image” resampling [68], [69]. Interpolation is a basic tool in the area of image processing, such as zooming, shrinking, etc. [67]. It is a process of using known data to estimate unknown data at specified locations. Next, we shall discuss how interpolation can be done using the DCT.

#### 3.3.1 Discrete Cosine Transform (DCT)

A Discrete Cosine Transform (DCT) is used to express data points as a sum of cosine functions oscillating at different frequencies, i.e., it helps separate the image into spectral sub-bands [68]. The general equation for the 1D DCT for an  $N$ -sample signal  $f[n]$  is as follows:

$$F[v] = \sqrt{\frac{2}{N}} c[v] \sum_{n=0}^{N-1} f[n] \cos\left(\frac{\pi(2n+1)v}{2N}\right), \quad 0 \leq v \leq N-1, \quad (26)$$

where  $n$  is a sampling instance, and  $c[v]$  is a normalization factor defined as follows:

$$c[v] = \begin{cases} 1/\sqrt{2}, & v = 0 \\ 1, & \text{otherwise} \end{cases} \quad (27)$$

The signal  $f[n]$  can be recovered from  $F[v]$  using the 1D Inverse Discrete Cosine Transform (IDCT) [68]:

$$f[n] = \sum_{v=0}^{N-1} c[v]F[v]\cos\left(\frac{\pi(2n+1)v}{2N}\right), \quad 0 \leq n \leq N-1. \quad (28)$$

In the case of  $M$ -by- $N$  2D signals  $f[m, n]$ , we have the following 2D DCT definition [68]:

$$F[u, v] = \frac{2}{\sqrt{MN}} c[u]c[v] \sum_{n=0}^{N-1} \sum_{m=0}^{M-1} f[m, n]\cos\left(\frac{\pi(2n+1)v}{2N}\right)\cos\left(\frac{\pi(2m+1)u}{2M}\right), \quad (29)$$

where for each  $u = 0, 1, \dots, M-1$ , the normalization factor  $c[u]$  is given by:

$$c[u] = \begin{cases} 1/\sqrt{2}, & u = 0 \\ 1, & \text{otherwise} \end{cases} \quad (30)$$

The 2D IDCT can be computed using the equation [68]:

$$f[m, n] = \sqrt{\frac{2}{N}} \sum_{v=0}^{N-1} c[v] \left\{ \frac{2}{\sqrt{M}} \sum_{u=0}^{M-1} c[u]F[u, v]\cos\left(\frac{\pi(2m+1)u}{2M}\right) \right\} \cos\left(\frac{\pi(2n+1)v}{2N}\right). \quad (31)$$

### 3.3.2 Interpolation via Zero Padding

It is well known that zero padding in the frequency domain corresponds to periodic interpolation in the time domain [68]. In other words, zero padding of the  $N$ -sample DCT representation  $F[v]$  by a factor of  $L$  corresponds to periodic interpolation of  $f[n]$  by the same factor  $L$  [69], [70]:

$$INTERP_{L,N}(f) = IDCT(2 \cdot ZEROPAD_{L,N}(F)), \quad (32)$$

where

$$ZEROPAD_{L,N}(F) = \begin{cases} F[v], & 0 \leq v < N \\ 0, & N \leq v < L \cdot N \end{cases} \quad (33)$$

For example, in our case, lowering the temporal sampling rate by the factor of  $L = 2$  yields 1D signal  $f[n]$  of length  $N_t/2$  for each sensor, from which we want to obtain  $INTERP_{L,N}(f)$  of length  $N_t$  (i.e.,  $L = 2$  and  $N = N_t/2$ ). To accomplish that, we compute  $F[v]$  of length  $N_t/2$ , add

zero padding to create  $ZEROPAD_{L,N}(F)$ , and then compute the length- $N_t$  IDCT of the result. Once we get the full-size raw ARFI data using such DCT-based interpolation, we apply the FDM method described in the previous section to obtain the corresponding beamformed data. We refer to this procedure as the DCT+FDM method.

# Chapter 4

## MATLAB Implementation

### 4.1 Overview of USTB

Ultrasound Toolbox (USTB) is an open source MATLAB package for processing ultrasonic signals [60]. The main aim of USTB is to serve as a common platform to compare various imaging and beamforming techniques, and to encourage the publication of relevant datasets and algorithms. The datasets in USTB are stored in Universal File Format (UFF) developed by SDRC (Structural Dynamics Research Co.) to regulate the transfer of data between CAD (Computer Aided Design) and CAT (Computer Aided Test) software packages.

Fig. 4.1 shows the block diagram of ARFI data processing in the USTB framework. The raw ARFI channel data is of size  $N_t \times N_x \times N_f$ , where  $N_t$  is the number of time samples,  $N_x$  is number of channels (sensors), and  $N_f$  represents number of frames acquired. The pre-process block includes a scan structure, which can be defined by the user. Next, the raw channel data is sent to the midprocess block, where beamforming takes place, followed by computing the IQ version of the beamformed data via the Hilbert transform. The resulting IQ data frame is then sent to the post-process block, where coherent compounding takes place. Coherent compounding refers to summing all the individual frames obtained at different plane-wave emission angles to form a final compounded beamformed frame. The main purpose of the coherent compounding is to improve the image quality.

Each beamformed and compounded IQ data frame produced by the post-process block is then fed into the envelope detection and log-compression block. The 2D envelope is calculated by simply taking the absolute value of the IQ data, followed by normalization to the maximum.

Log-compression refers to computing  $20 \cdot \log_{10}(X)$ , where  $X$  denotes the normalized envelope, which is then used for the B-mode image display. The beamformed and compounded IQ data frames (forming a sequence) are also used by the displacement estimation block. It performs 2D displacement calculations among the successive frames, and its results can be viewed as a video showing how the displacement estimates change over the duration of the frame sequence.

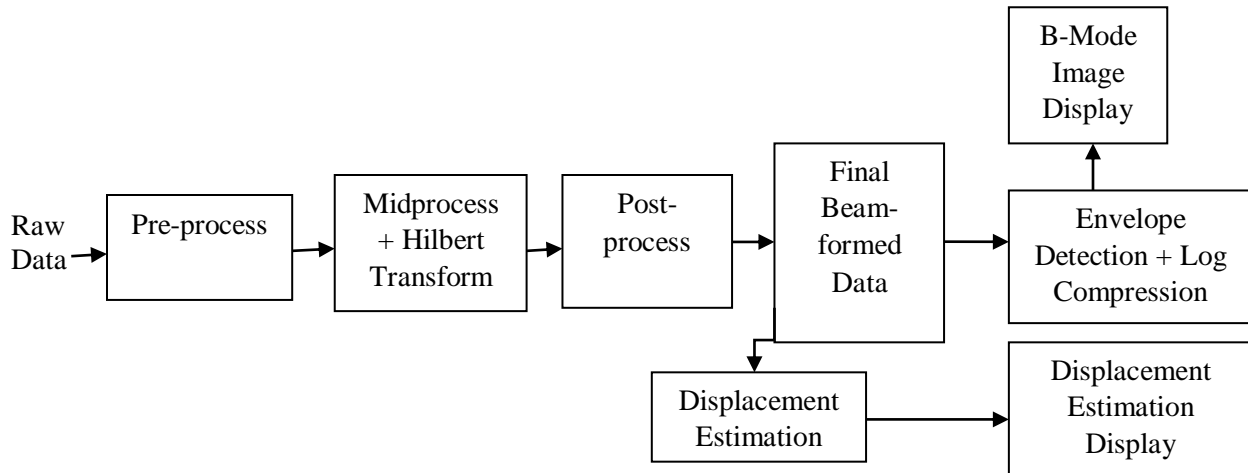


**Fig. 4.1.** Block diagram of ARFI data processing.

## 4.2 Midprocess Implementation

The USTB package provides the reference implementation of DAS beamforming as the default midprocess block. In this work, we have implemented an alternative midprocess step that replaces DAS beamforming with the faster FDM method. Its corresponding pseudo-code snippet is shown in Fig. 4.2 (recall section 3.2). Here, `RFdata` is the 2D raw channel data (for a given emission PW angle  $\theta$ , indexed by `Ind_f`), `F` refers to the temporal frequencies, `Kx` and `Kz` refer to the spatial frequencies in relation to the  $x$ -axis and  $z$ -axis, respectively (`NtFFT` and `NxFFT` are the temporal and spatial FFT sizes), `cs` is speed of sound (1540 m/s), and `intF` denotes the frequency interpolation points (we use spline interpolation in this work).

```

D_t_x = RFdata(Ind_f);
%-- Step 1
D_F_x = fft(D_t_x, NtFFT);
D_F_Kx = fft(D_F_x, NxFFT, 2);
D_F_Kx_Shifted = fftshift(D_F_Kx, NxFFT, 2);
%-- Step 2
K_z = F/c_s;
K_new = K_z.*(1 + (K_x/K_z).^2);          K_new(isnan(K_new)) = 0;
intF = c_s*K_new(1 + cos(theta))/2;      % Interpolation points
for i = 1:NxFFT
    D_K_z_K_x_Interpolated(:,i) = ...
        interpolate(F(i), D_F_Kx_Shifted(:,i), intF(i));
end
scaler = c_s*(1 - (K_z./K_x).^2)/(1 + cos(theta));
negative = (K_z.^2 <= K_x.^2);
scaler(negative) = 0;
D_K_z_K_x = scaler.* D_K_z_K_x_Interpolated;
%-- Step 3
D_K_z_K_x_Shifted = ifftshift(D_K_z_K_x, 2);
D_K_z_x = ifft(D_K_z_K_x_Shifted, NxFFT, 2);
for i = 1:Nx
    D_K_z_x(:,i) = D_K_z_x(:,i).*exp(j*pi*K_z*x(i)*tan(theta));
end
%-- Step 4
D_z_x = ifft(D_K_z_x, NtFFT, 'symmetric');

```

**Fig. 4.2.** Pseudo-code for FDM method.

For each plane wave, we apply 2D FFT on the corresponding raw channel data  $D_{t_x}$ , followed by the FFT shift to get our  $K_x$ -centered 2D spectrum  $D_{F_{K_x} \text{ Shifted}}$ . Next, we perform spline interpolation on it along the F-axis to obtain  $D_{K_z K_x \text{ Interpolated}}$ , followed by element-wise multiplications using the scaling factor  $scaler$ . Then, we undo the earlier FFT shift and compute the 1D IFFT along the  $K_x$ -axis, which produces the intermediate migrated spectrum  $D_{K_z_x}$ . This is followed by applying the appropriate  $x$ -dependent phase shifts  $\exp(j * \pi * K_z * x * \tan(\theta))$ . Finally, we apply the 1D IFFT to get our beamformed data frame  $D_{z_x}$ .

### 4.3 DCT-Based Interpolation

Fig. 4.3 shows the pseudo-code snippet for the DCT+FDM method mentioned in section 3.3. We reduce the temporal sampling frequency by the factor of  $L = 2$ , which means that each raw data frame  $D_{t_x \text{ Subsampled}}$  is of size  $N_t/2 \times N_x$ . Next, we apply the 1D DCT along the  $t$ -axis to obtain  $D_{DCT_x}$ , followed by zero padding to increase the size of the resulting data frame  $D_{DCT_x \text{ Zeropadded}}$  to  $N_t \times N_x$ . Then, by computing the 1D IDCT of the said zero-padded data, we obtain the interpolated data frame  $D_{t_x}$ . Finally, we apply steps 1-4 from Fig.4.2 to complete the beamforming process.

```

L = 2;
D_t_x_Subsampled = subsample(RFdata(Ind_f), L);

D_DCT_x = dct(D_t_x_Subsampled);
D_DCT_x_Zeropadded = [2* D_DCT_x; zeros(Nt/L, Nx)];
D_t_x = idct(D_DCT_x_Zeropadded);

Run Steps 1-4 from Fig. 4.2;

```

**Fig. 4.3.** Pseudo-code for DCT+FDM method.

### 4.4 Displacement Calculation

After applying the DAS, FDM, or DCT+FDM methods, we have the 3D beamformed dataset  $Y$  of size  $N_r \times N_c \times N_f$ , where  $N_r = N_t$  is the number of rows (representing the  $z$ -axis),  $N_c = N_x$  is number of columns (representing the  $x$ -axis), and  $N_f$  is the total number of frames in an ARFI image sequence. The “analytic” representation of  $Y[m, n, o]$  is defined as [62]:

$$Y_+[m, n, o] = Y[m, n, o] + j \{ Y_H[m, n, o] \}, \quad (34)$$

where indices  $m$ ,  $n$ , and  $o$  refer to the particular row, column, and frame numbers, respectively, and  $Y_H$  is the 1D Hilbert transform of  $Y$  along the  $z$ -axis.

To calculate displacement estimates, we first need to find an autocorrelation estimate  $Y_{\text{autocorr}}$  of  $Y_+$  at any given point  $[m, n, o]$ . This can be accomplished in three consecutive steps [43], [62]:

$$Y_{\text{autocorr}}[m, n, o] = \sum_{k=o-W+1}^{o-1} Y_+[m, n, k] Y_+^*[m, n, k+1], \quad (35)$$

$$Y_{\text{autocorr}}[m, n, o] = \sum_{i=m-\lfloor \frac{U-1}{2} \rfloor}^{m+\lfloor \frac{U-1}{2} \rfloor} Y_{\text{autocorr}}[i, n, o], \quad (36)$$

$$Y_{\text{autocorr}}[m, n, o] = \sum_{j=n-\lfloor \frac{V-1}{2} \rfloor}^{n+\lfloor \frac{V-1}{2} \rfloor} Y_{\text{autocorr}}[m, j, o], \quad (37)$$

where  $Y_+^*$  denotes the complex conjugate of  $Y_+$ ,  $U$  is the axial gate range,  $V$  is the lateral gate range, and  $W$  is the frame ensemble length [62]. Then, we have

$$f_{\text{doppler}} = \frac{\tan^{-1}(\text{Im}(Y_{\text{autocorr}})/\text{Re}(Y_{\text{autocorr}}))}{2\pi}, \quad (38)$$

$$d[m, n, o] = \frac{c_s \cdot f_{\text{doppler}}}{2f_c}, \quad (39)$$

where  $f_{\text{doppler}}$  represents the Doppler frequency calculated from autocorrelation,  $d$  is our desired displacement estimate, and  $f_c$  represents the PW pulse center frequency. In this work, we have used the implementation of the above estimation method, as provided in the USTB package.

# Chapter 5

## Evaluation Results

### 5.1 Description of ARFI Phantom

Our evaluation results are based on the public-domain USTB experimental dataset acquired from the CIRS QA Spherical Phantom [51]. This phantom contains eight spheres, as depicted in Fig. 5.1, classified into four types. Type I, Type II, Type III, and Type IV spheres have Young's modulus values of 8 KPa, 14 KPa, 45 KPa, and 80 KPa, respectively. The background has Young's modulus value of 25 KPa. The bigger spheres are 20 mm in diameter, and the smaller ones are 10 mm in diameter.

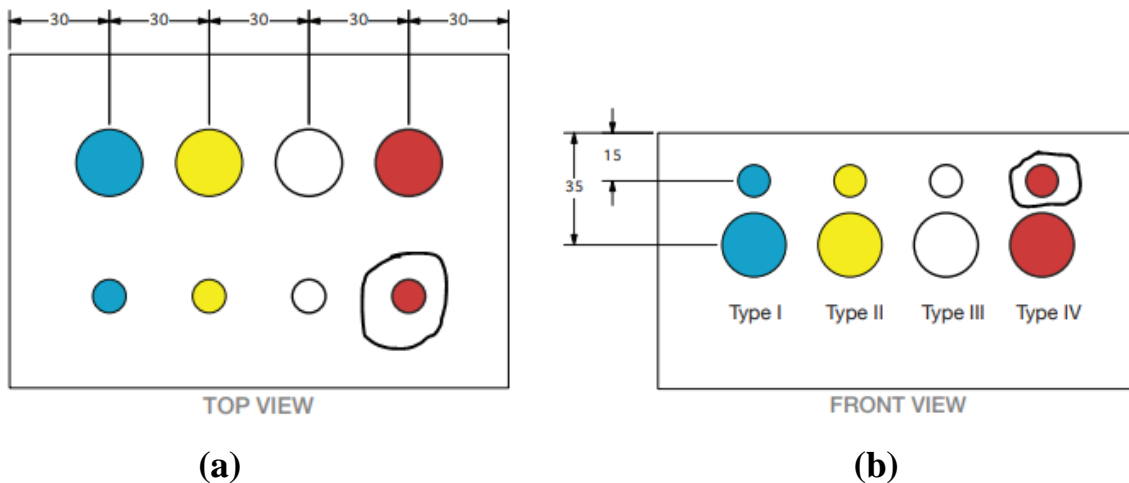


**Fig. 5.1.** (a). Top view of Spherical Phantom, highlighted is the imaged sphere, (b). Front view of Spherical Phantom, highlighted is the imaged sphere [51].

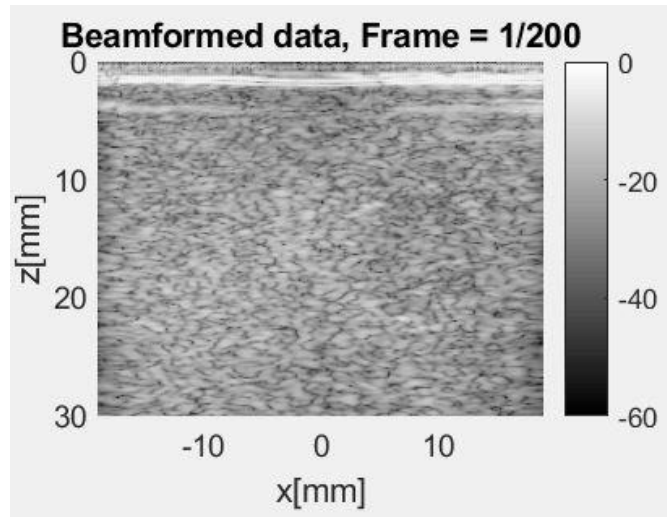
In our work, we used the ARFI dataset that corresponds to the phantom section containing the 10-mm sphere of Type IV (outlined in the above figure). The raw channel samples of this dataset were acquired by the Verasonics research scanner using a 128-element probe [61]. There are four so-called super frames, each consisting of 50 regular frames tracking shear-wave displacements

after an ARFI push created at the beginning of each super frame. The size of the dataset is  $1664 \times 128 \times 200$ , where  $N_t = 1664$  is the number of temporal samples,  $N_x = 128$  is number of sensors, and  $N_f = 200$  is the total number of frames.

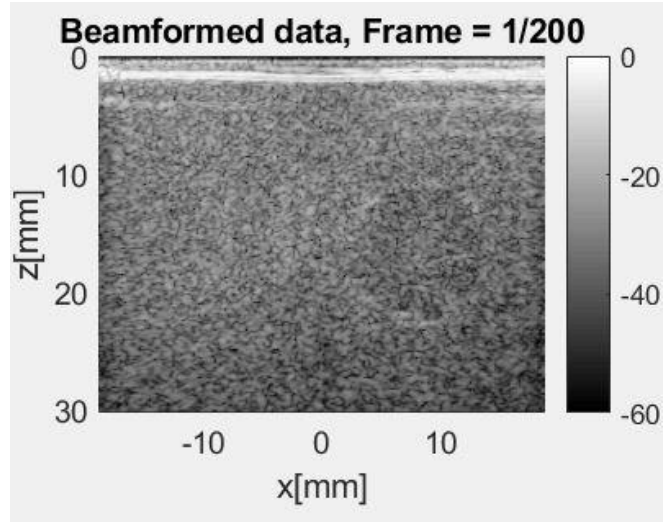
## 5.2 Imaging Results

A B-mode image is generated from the beamformed data as follows. First, the beamformed data is converted into its “analytical” representation (see Equation (34) in Section 4.4). Taking the absolute value of the latter yields a 2D envelope, which is then normalized to its maximum value. This max-normalized envelope  $X$  undergoes log-compression by computing  $20 \cdot \log_{10}(X)$ , which is finally displayed as the B-mode image using some user-chosen dB range.

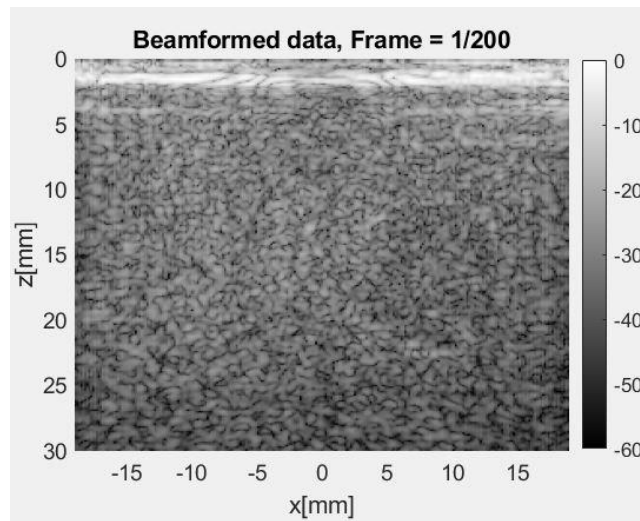
Fig. 5.2 shows the B-mode images obtained using the DAS, FDM and DCT+FDM methods under consideration. Our target sphere is barely visible at about  $x = 10$  mm and  $z = 15$  mm, which indicates that B-mode imaging is not suitable for elastographic applications.



(a)



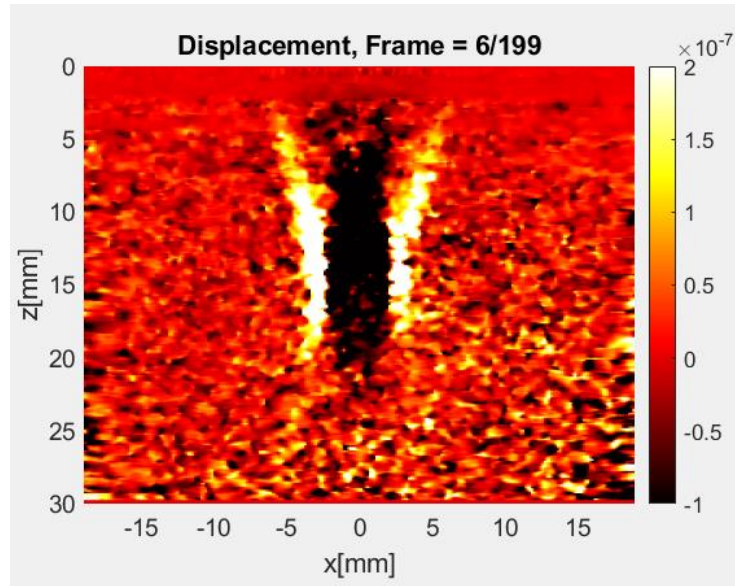
(b)



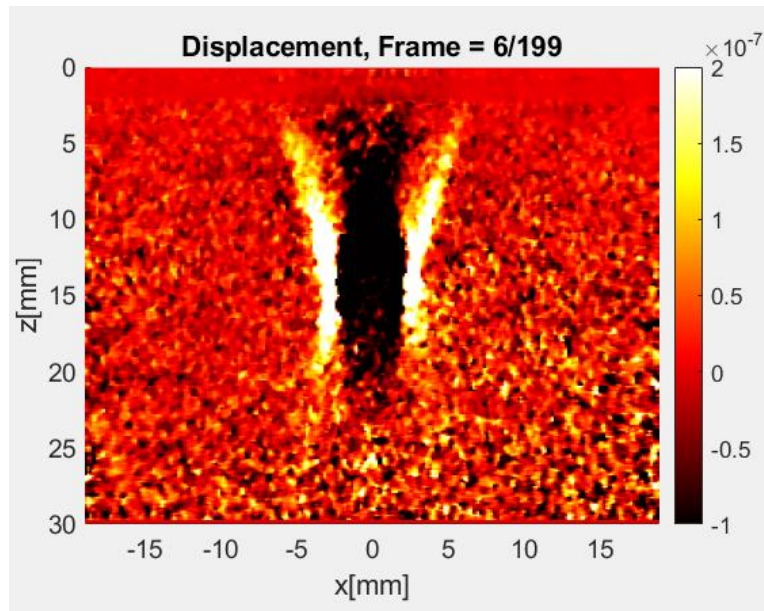
(c)

**Fig. 5.2.** B-Mode images for (a) DAS, (b) FDM and (c) DCT+FDM.

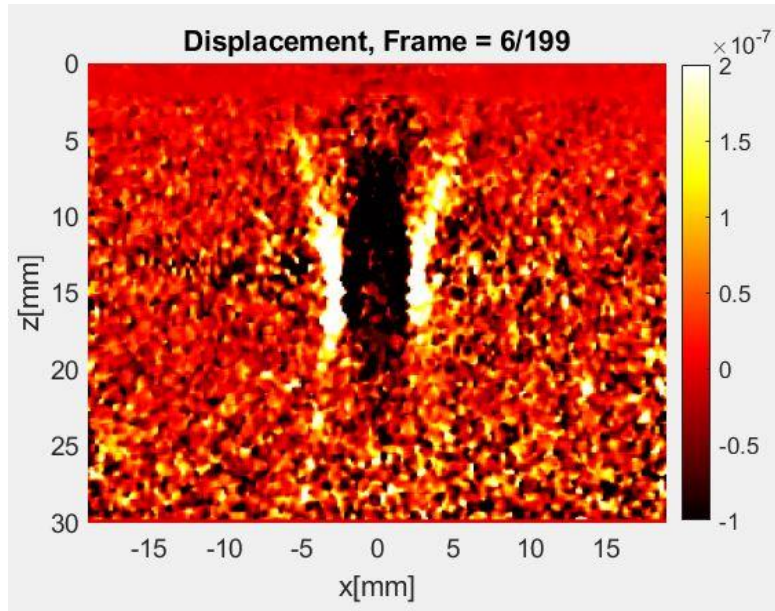
Next, we show several representative figures depicting displacement estimation results using  $U = 4$  and  $V = 2$ . Among the 200 frames in question, we have chosen frames 6, 12, 18, 24, 30, 36, and 42 (from the first super frame) to illustrate the effect of using DAS-based, FDM-based, and DCT+FDM-based image reconstruction.



(a)

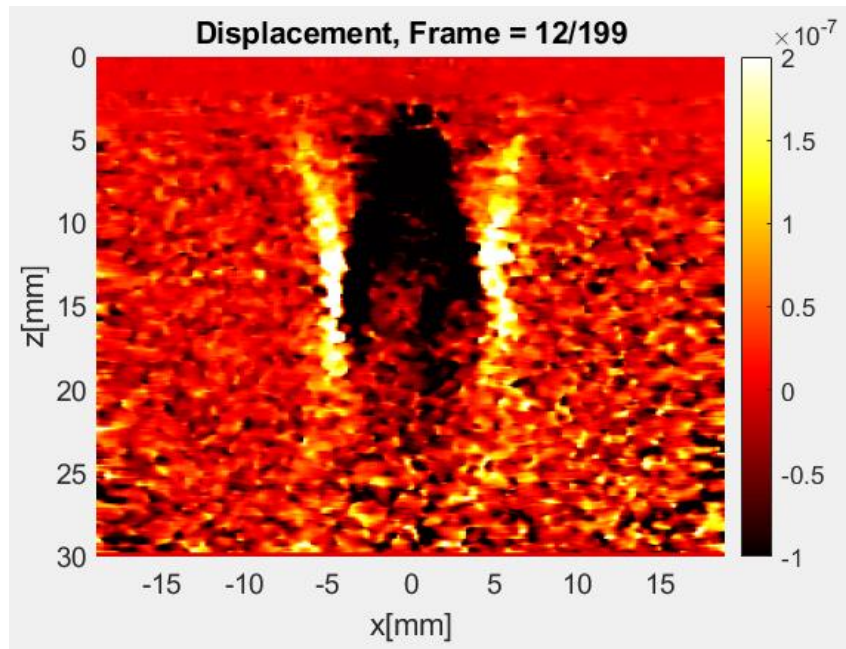


(b)

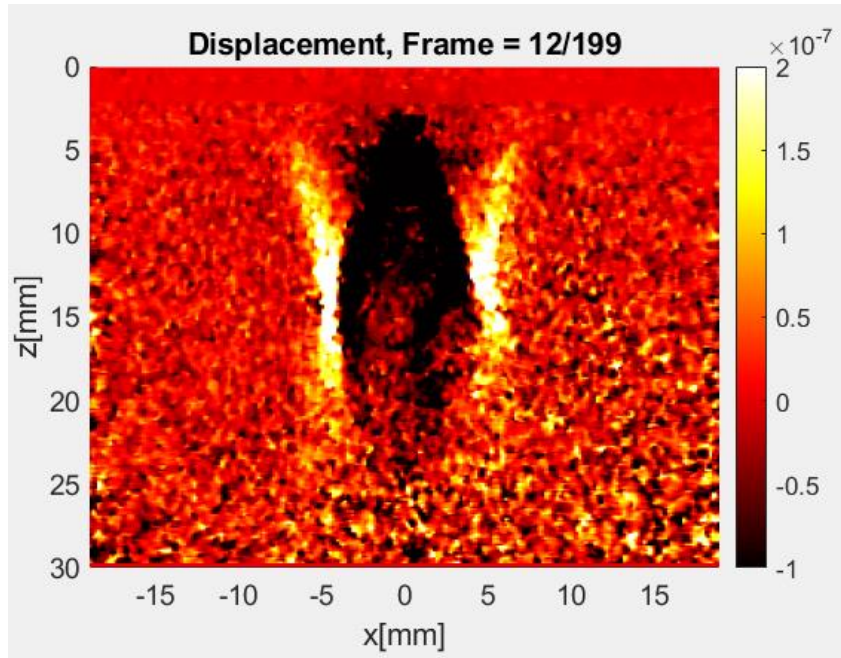


(c)

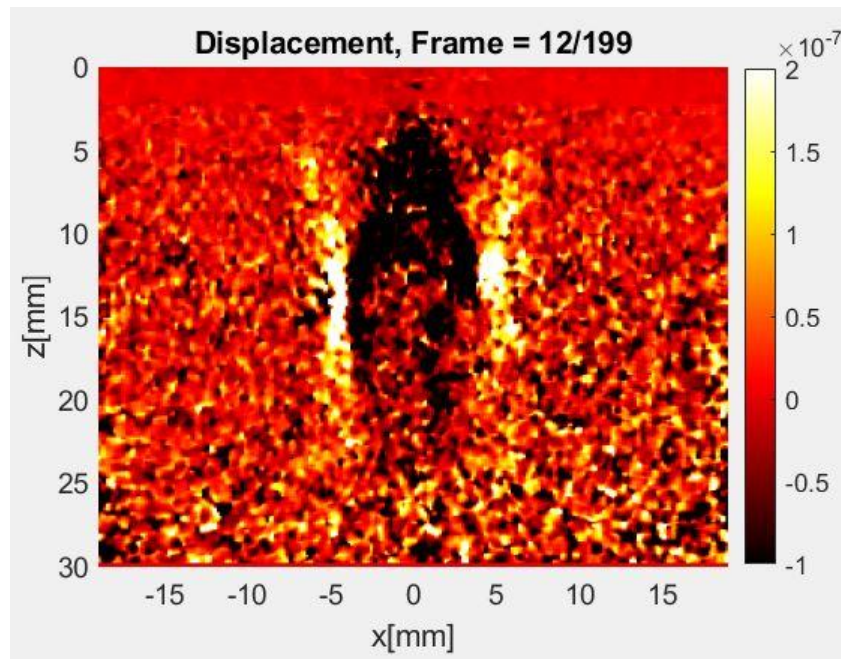
**Fig. 5.3.** Displacement images for (a) DAS, (b) FDM and (c) DCT+FDM: Frame 6



(a)

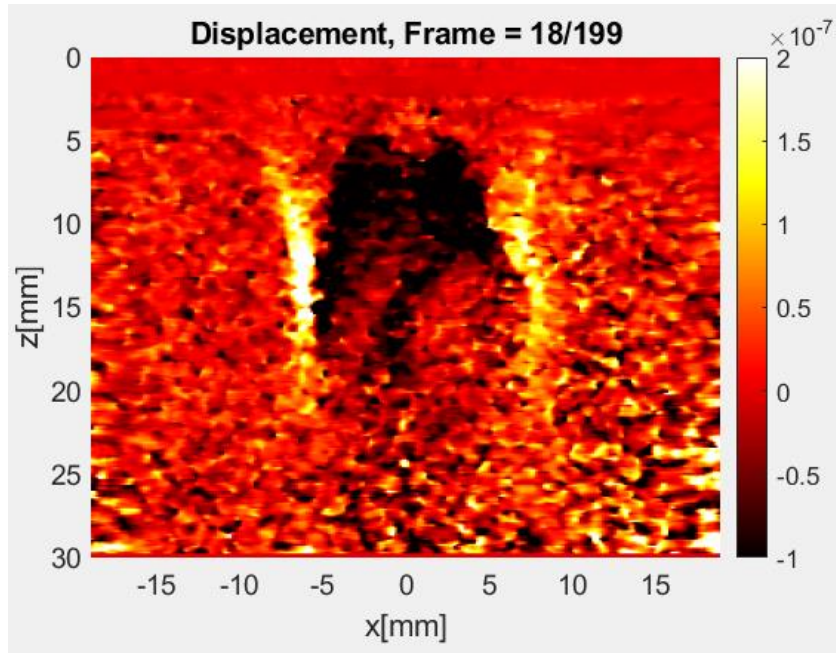


(b)

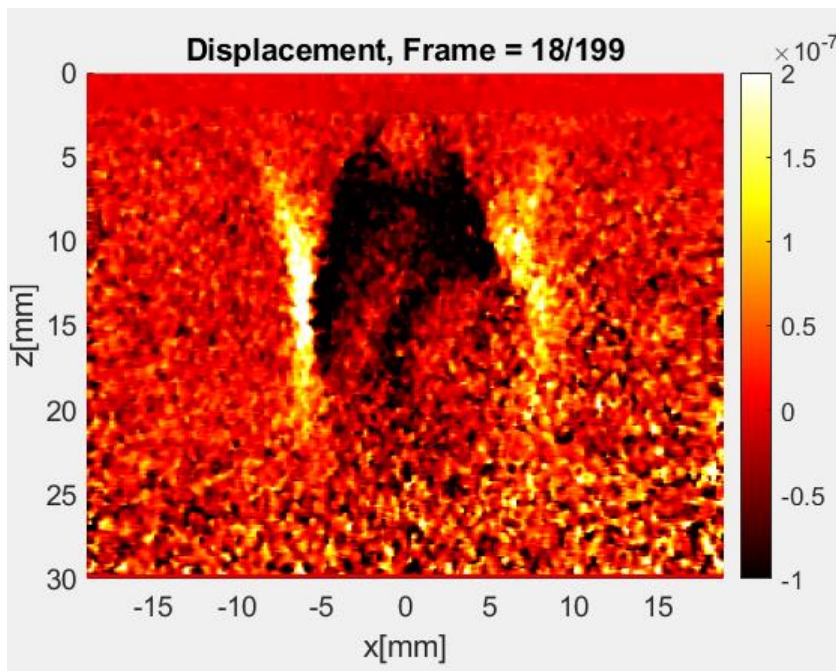


(c)

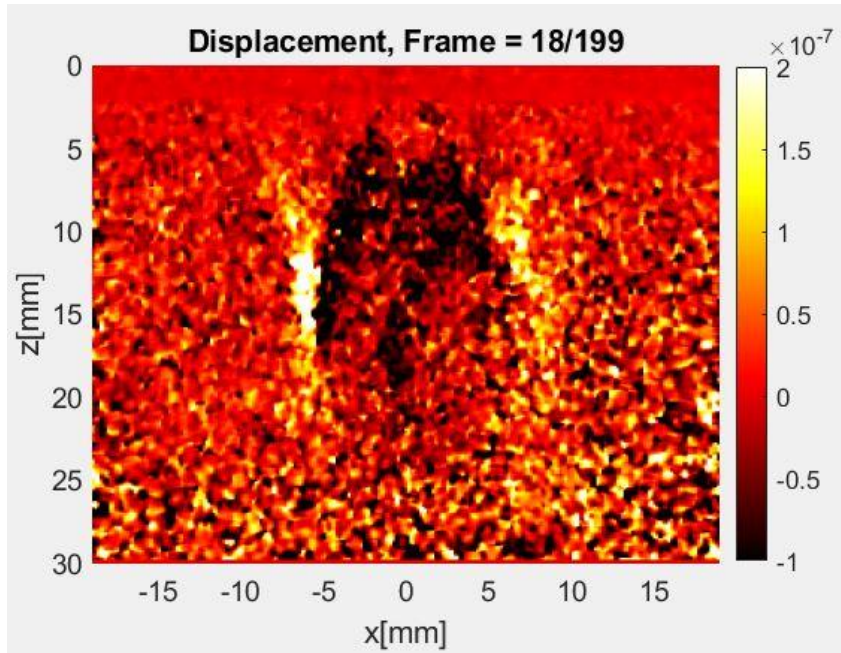
**Fig. 5.4.** Displacement images for (a) DAS, (b) FDM and (c) DCT+FDM: Frame 12



(a)

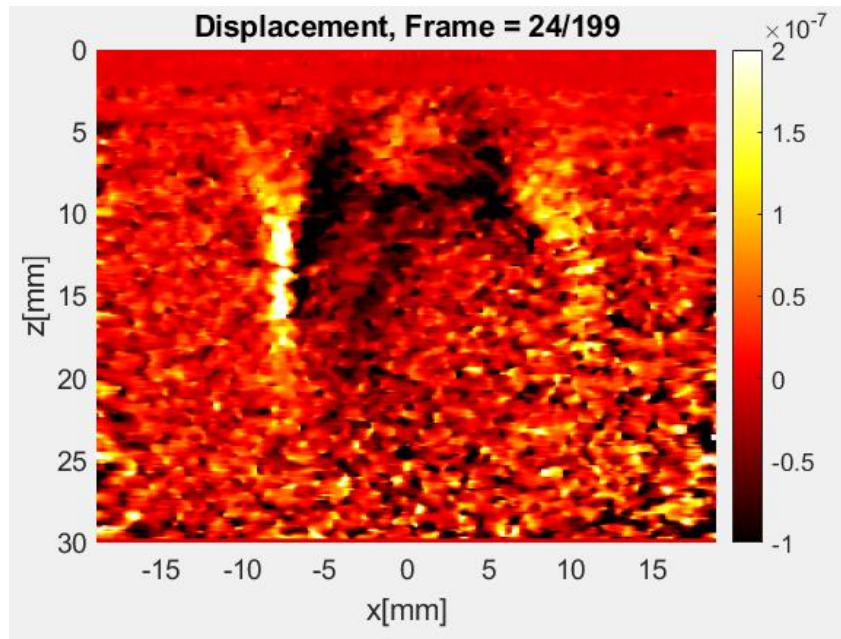


(b)

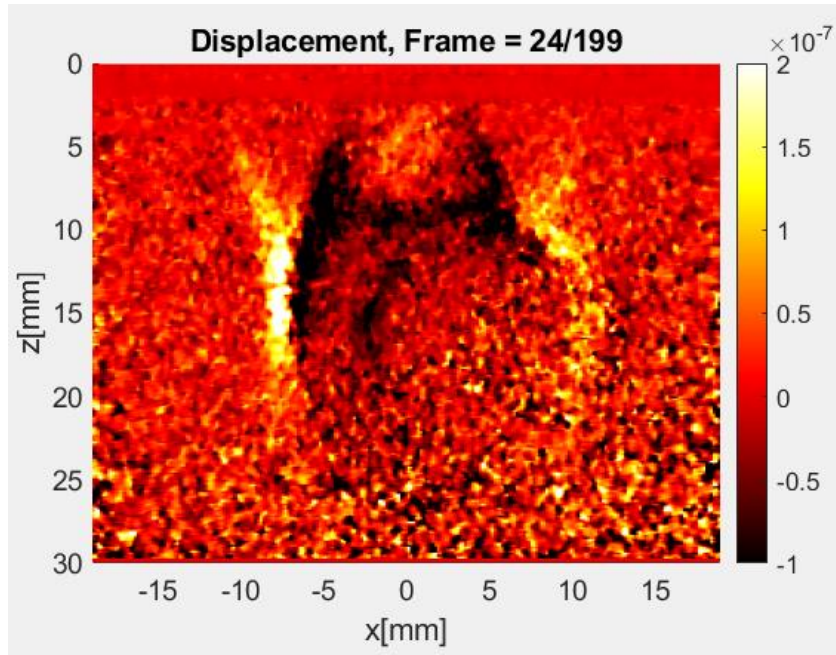


(c)

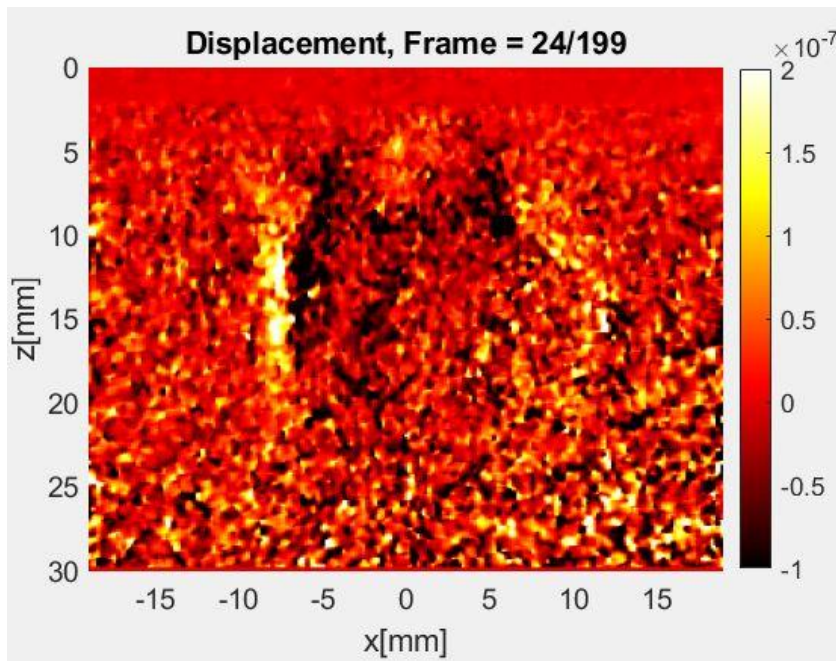
**Fig. 5.5.** Displacement images for (a) DAS, (b) FDM and (c) DCT+FDM: Frame 18



(a)

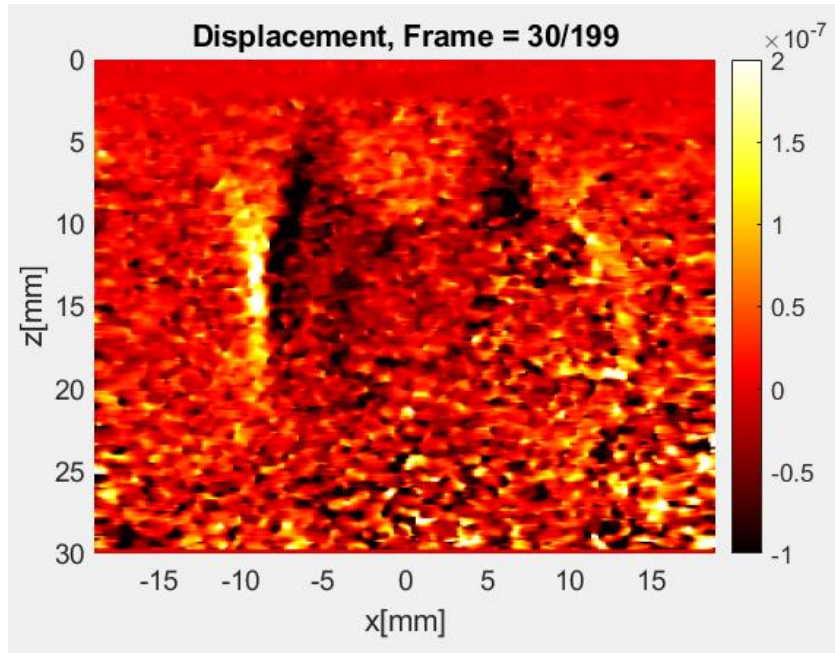


(b)

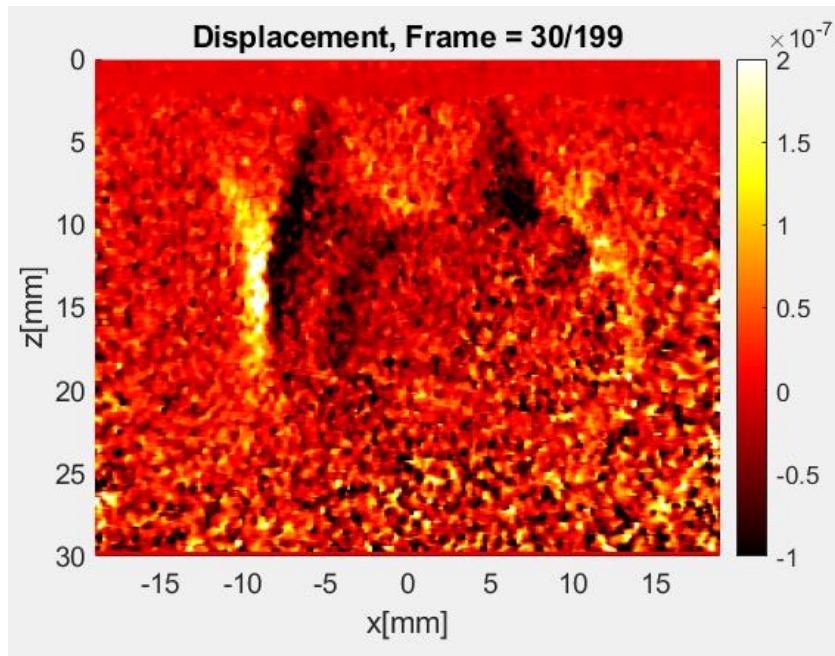


(c)

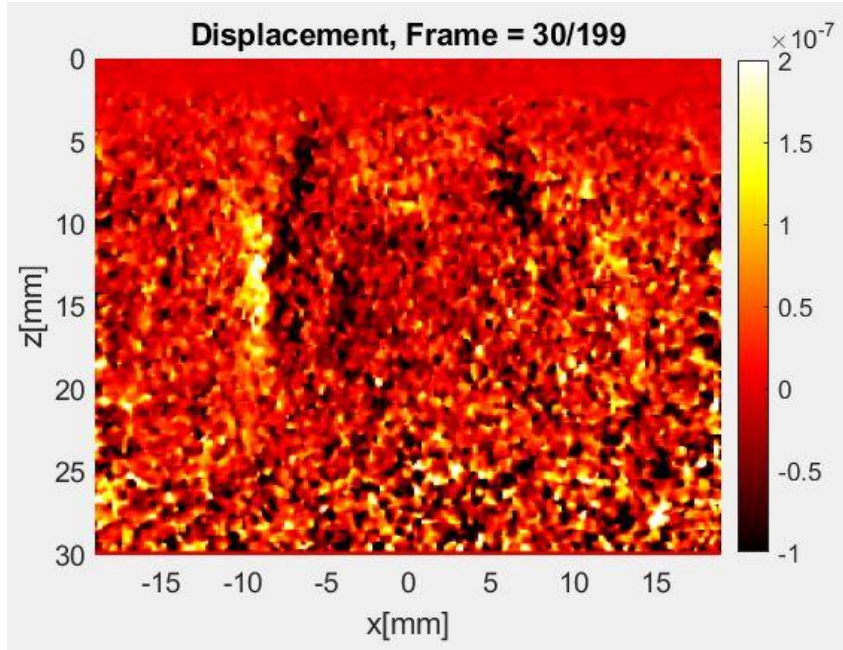
**Fig. 5.6.** Displacement images for (a) DAS, (b) FDM and (c) DCT+FDM: Frame 24



(a)

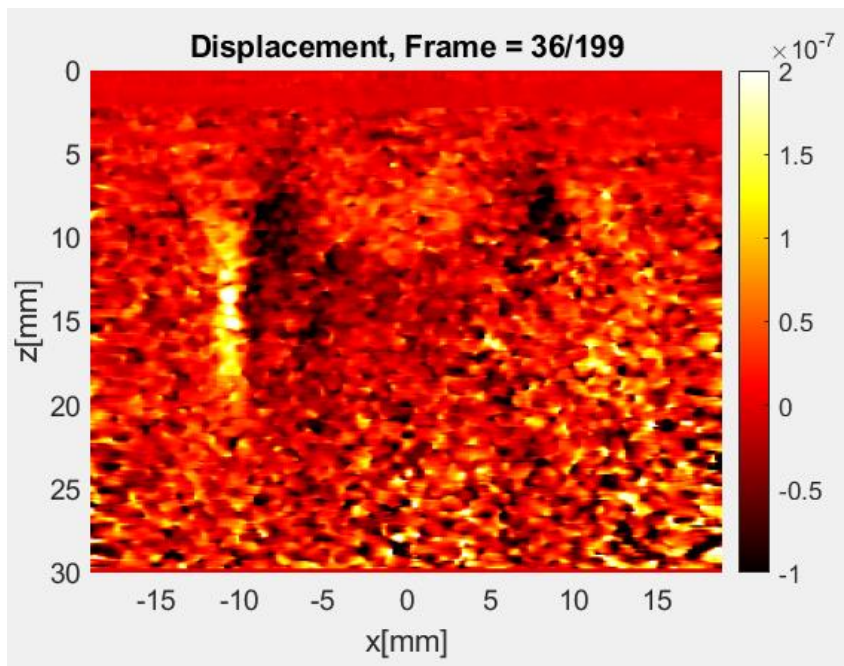


(b)

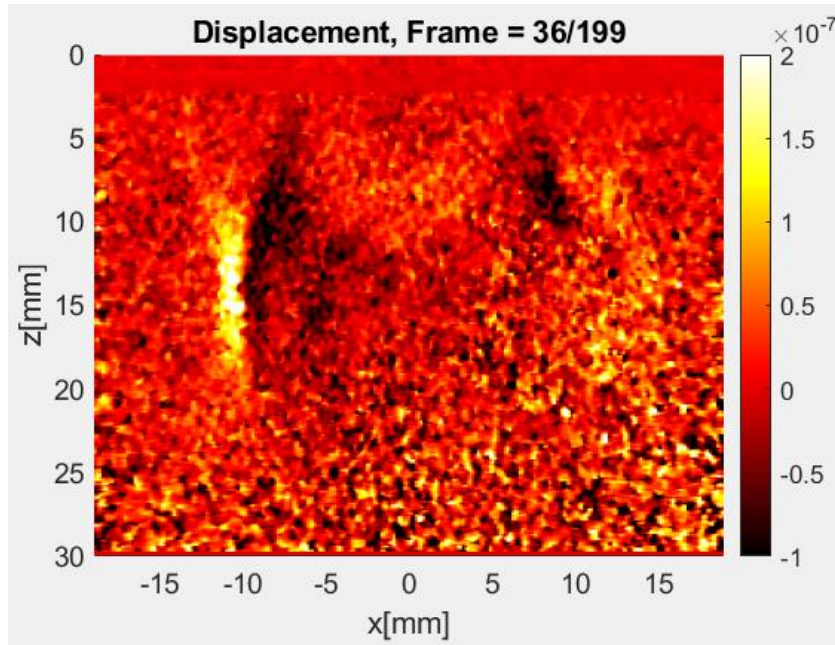


(c)

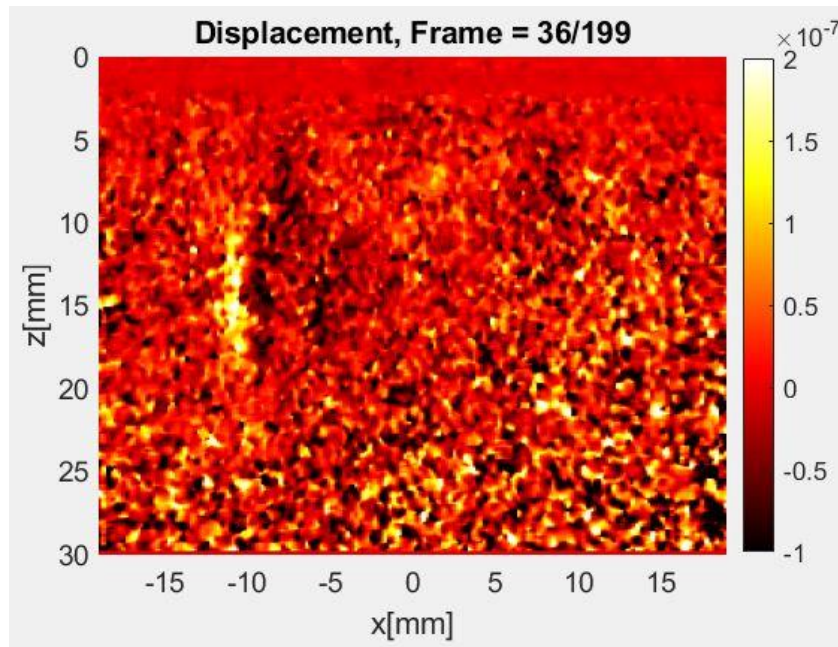
**Fig. 5.7.** Displacement images for (a) DAS, (b) FDM and (c) DCT+FDM: Frame 30



(a)

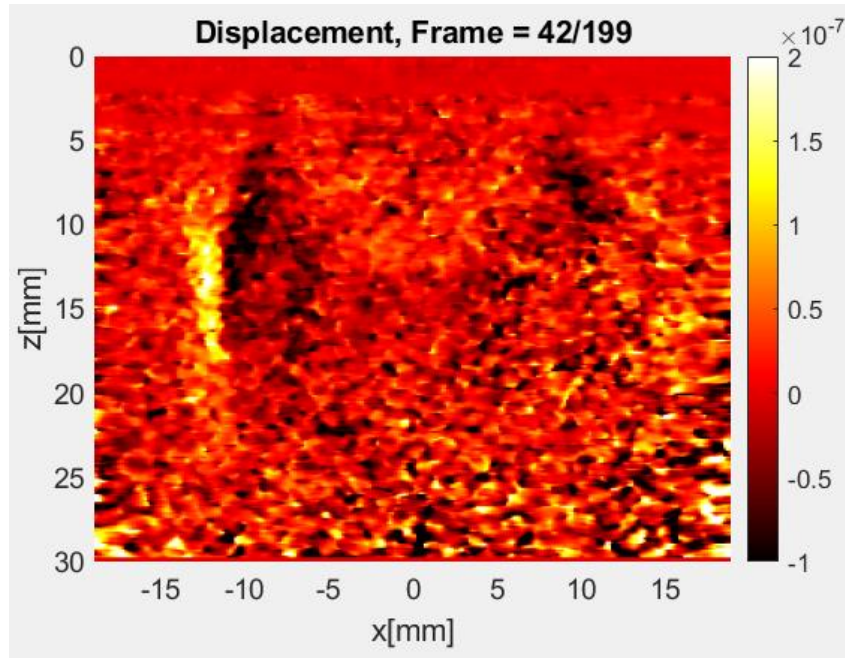


(b)

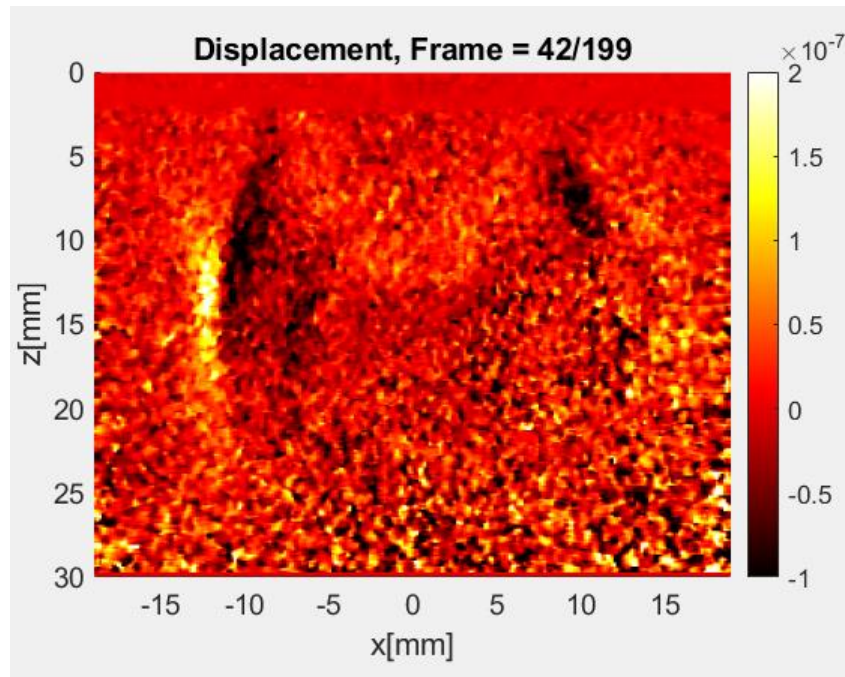


(c)

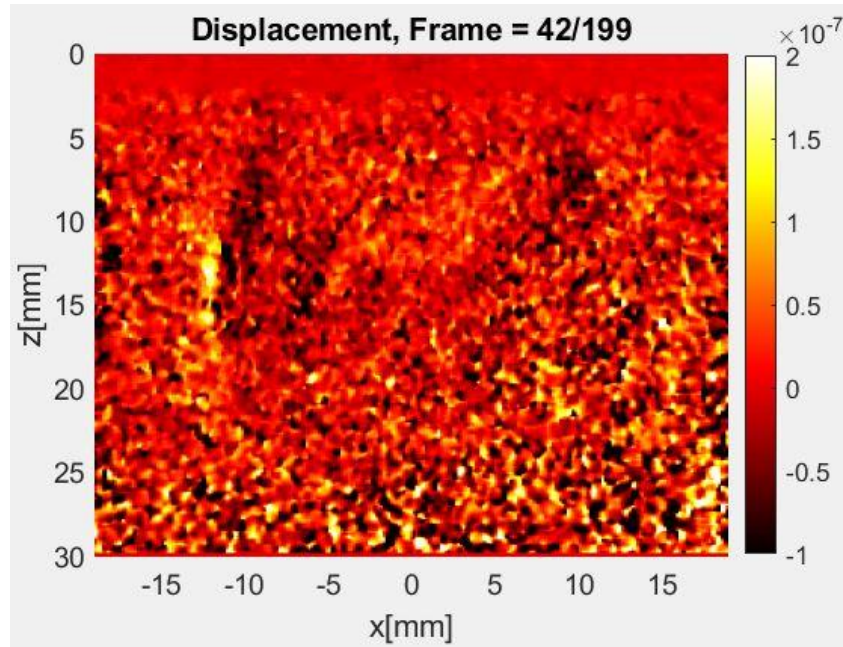
**Fig. 5.8.** Displacement images for (a) DAS, (b) FDM and (c) DCT+FDM: Frame 36



(a)



(b)



(c)

**Fig. 5.9.** Displacement images for (a) DAS, (b) FDM and (c) DCT+FDM: Frame 42

### 5.3 Similarity of Displacement Images

Figs. 5.3-5.9 show that the DAS and FDM methods produce very similar images; however, the DCT+FDM method yields noticeably different displacement estimates. Table 5.1 provides a quantitative comparison of the displacement images using the SSIM metric. The SSIM values between the DAS (reference) and FDM images are above 0.9. On the other hand, the SSIM values between the FDM (reference) and DCT+FDM images is below 0.9, which is consistent with the observation that the visual similarity between DAS and FDM cases is higher than that between FDM and DCT+FDM cases. Also note that the displacement images toward the end of a super-frame sequence become more similar, as the transient deformation response gradually dies out.

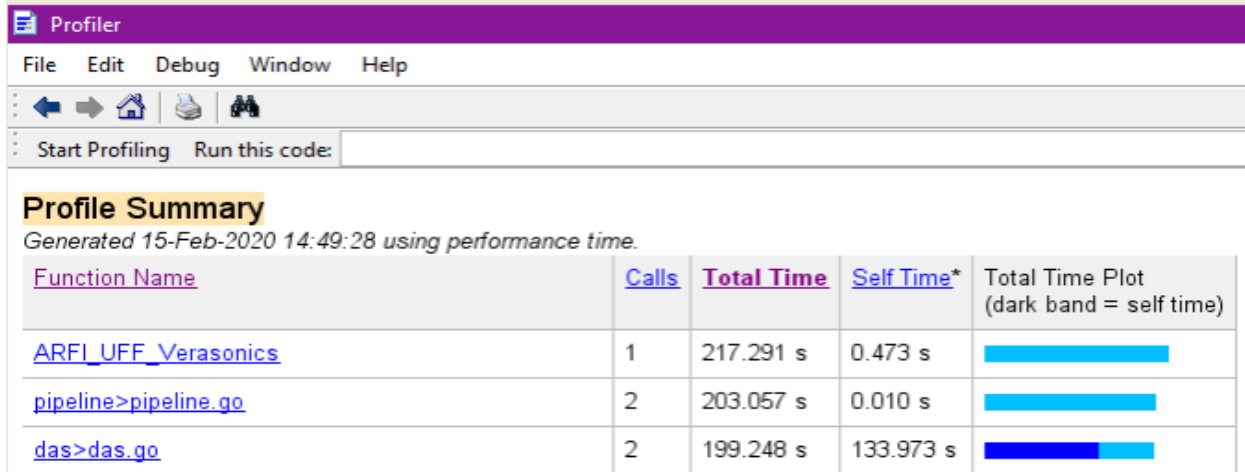
Frame Number	SSIM between DAS (Reference) and FDM Images	SSIM between FDM (Reference) and DCT+FDM Images
Frame 6	0.9010	0.8664
Frame 12	0.9035	0.8641
Frame 18	0.9025	0.8718
Frame 24	0.9143	0.8793
Frame 30	0.9173	0.8858
Frame 36	0.9219	0.8889
Frame 42	0.9227	0.8918

**Table 5.1.** Similarity of displacement images for DAS, FDM and DCT+FDM methods.

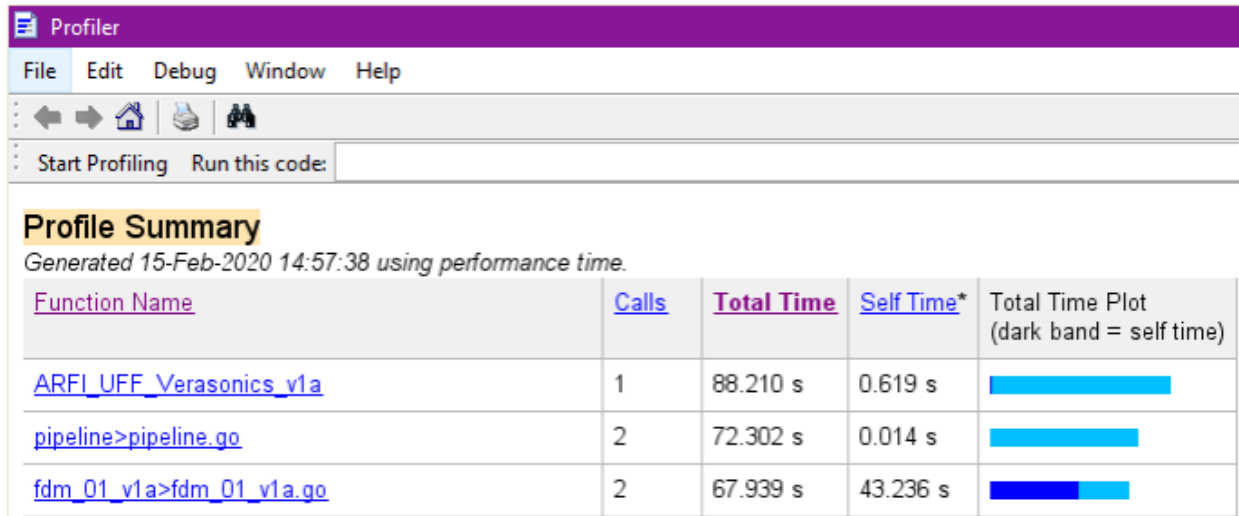
## 5.4 Comparison of MATLAB Timing Profiles

Fig. 5.10 below shows MATLAB timing values for DAS, FDM, and DCT+FDM methods, obtained when running our USTB code on a computer with the following specifications:

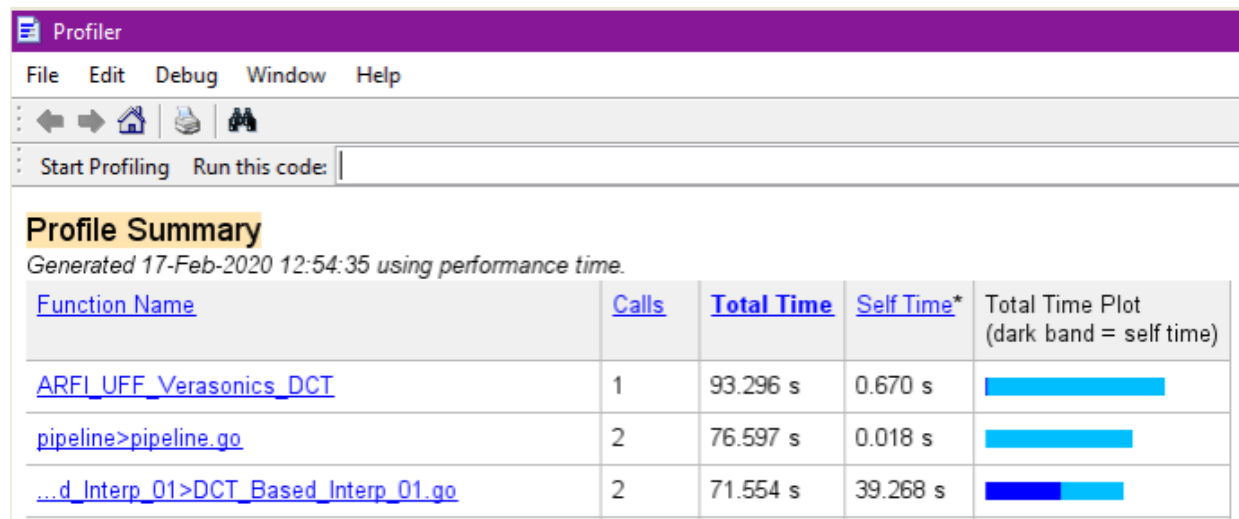
- Program version: MATLAB 2019b, USTB v1.2, 64-bit Windows 10 Enterprise;
- Processor: Intel® Core™ 2.20-GHz i7-3632QM CPU;
- Installed RAM: 8.00 GB (7.90 GB usable).



(a)



(b)



(c)

**Fig. 5.10.** MATLAB timing profiles for (a) DAS, (b) FDM and (c) DCT+FDM methods.

From Figs. 5.10 (a) and (b), one can see that the FDM method is considerably faster than the DAS method (67.939 seconds vs. 199.248 seconds). Using DCT interpolation allows for 50% savings in terms of temporal samples acquired per frame; however, it entails additional computational cost. According to Fig. 5.10 (c), this cost is not significant: the DCT+FDM methods take 71.554 seconds, which is only 5.32% slower than the FDM method itself.

The runtime complexity of DAS beamforming is  $O(N_t N_x N_s)$  per image frame, where  $N_s$  represents the number of scan lines (which is equal to  $N_x$  in this work). On the other hand, the complexity of FDM is  $O(N_t N_x \log(N_t N_x))$ , which is determined by the dominating cost of 2D FFT/IFFT computations. This explains why FDM is faster than DAS beamforming [71].

# Chapter 6

## Elasticity Imaging

In the previous chapter, we have shown displacement images arising from the DAS, FDM, and DCT+FDM beamforming methods. These images are of limited value when used directly, as we are ultimately interested in Young's modulus (elasticity) estimates for the imaged section. In this chapter, we describe how we have obtained the desired elasticity images, or elastograms.

### 6.1 Stiffness Quantification via Shear Wave Imaging

The main equation used for calculation of shear wave velocity is [57]:

$$c_T = \sqrt{\mu/\rho}, \quad (40)$$

where  $c_T$  is shear wave speed (SWS),  $\mu$  is shear modulus, and  $\rho$  is material density. Using this equation, one can determine the speed of a shear wave (e.g., assuming the density value of 1000 kg/m<sup>3</sup>). SWS can be calculated using the time-of-flight (TOF) approach. This method has been used in ARF-based Shear Wave Elasticity Imaging (SWEI) by multiple groups [56, 57, 58]. Figs. 6.1 and 6.2 illustrate the principle of this technique by a simple example.

Recalling Figs. 5.2-5.9 from the previous chapter, we have picked the horizontal line at the approximate push focus depth of 14 mm, and five points on that line located at 2, 4, 6, 8, and 10 mm away from the push. Fig 6.1 shows the displacement time profiles at these locations. The shear wave arrival time can be determined from such profiles using time-to-peak (TTP) displacement calculations [57]. The time instances at which the corresponding five peaks occur are the arrival times of interest (see Fig. 6.1): they are 0.1667 ms, 0.75 ms, 1.083 ms, 1.583 ms, and 1.833 ms, respectively.

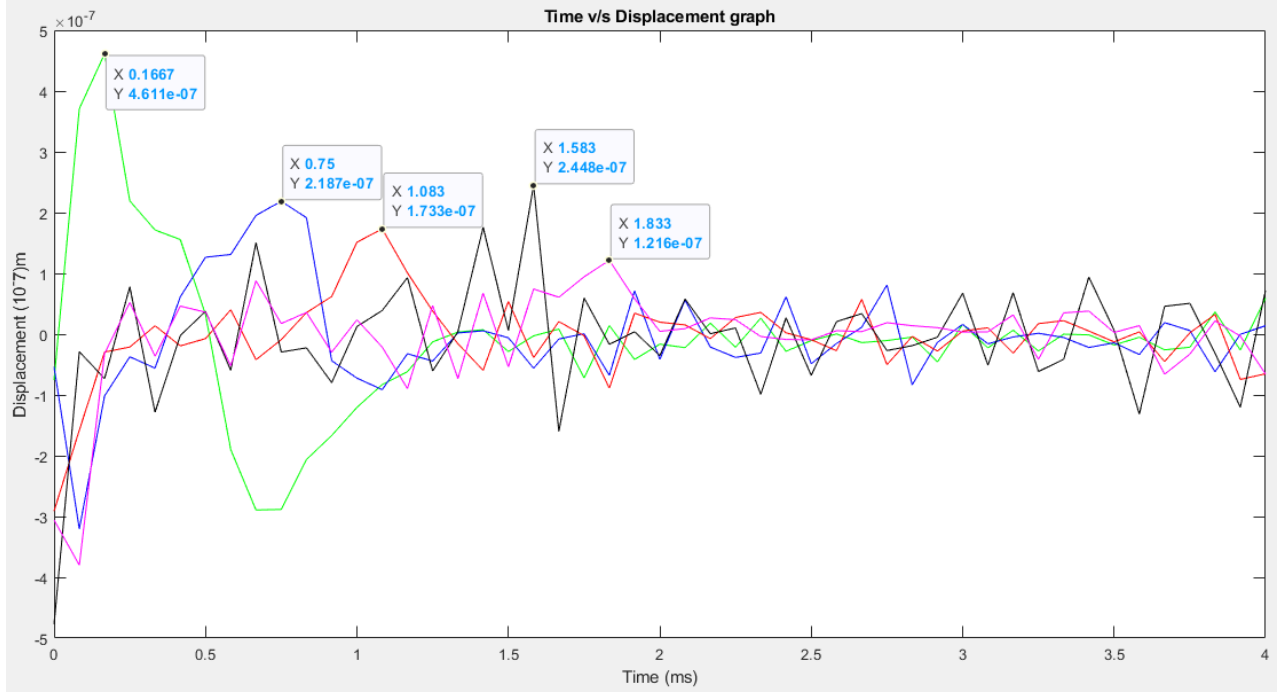


**Fig. 6.1.** Displacement time profile plotted for five chosen locations at various distances (2, 4, 6, 8, and 10 mm) away from the push. The first green peak (at 0.1667 ms), second blue peak at (0.75 ms), third red peak (at 1.083 ms), fourth black peak (at 1.583 ms), and fifth magenta peak (at 1.833 ms) correspond to the locations that are 2, 4, 6, 8, and 10 mm away from the push, respectively.

Assuming the lateral direction of propagation, the SWS value can be estimated using linear regression of lateral distance versus arrival time [65]. In our example, we have:

$$\mathbf{X} = \begin{pmatrix} x_1 & 1 \\ x_2 & 1 \\ x_3 & 1 \\ x_4 & 1 \\ x_5 & 1 \end{pmatrix}, \quad \mathbf{Y} = \begin{pmatrix} y_1 \\ y_2 \\ y_3 \\ y_4 \\ y_5 \end{pmatrix}, \quad \mathbf{W} = \begin{pmatrix} w \\ b \end{pmatrix}, \quad (41)$$

where  $x_1, x_2, x_3, x_4, x_5$  are lateral distances (i.e., 2, 4, 6, 8, 10 mm), and  $y_1, y_2, y_3, y_4, y_5$  are arrival times (i.e., 0.1667, 0.75, 1.083, 1.583, 1.833 ms). Our goal is to determine the unknown slope  $w$  and y-intercept  $b$  from the following equation (see Fig. 6.2):

$$\mathbf{Y} = \mathbf{XW}, \quad (42)$$

whose solution is given by

$$\mathbf{W} = (\mathbf{X}^T \mathbf{X})^{-1} (\mathbf{X}^T \mathbf{Y}). \quad (43)$$

In the resulting vector  $\mathbf{W}$ , the value of  $1/w$  is our SWS estimate  $c_T$ . We can now apply Eq. (40) to find shear modulus  $\mu$ , by squaring  $c_T$  and then multiplying by  $\rho$  (assumed equal to  $1000 \text{ kg/m}^3$ ). Using the relation  $E = 3\mu$  [52], we can determine the estimate of Young's modulus.

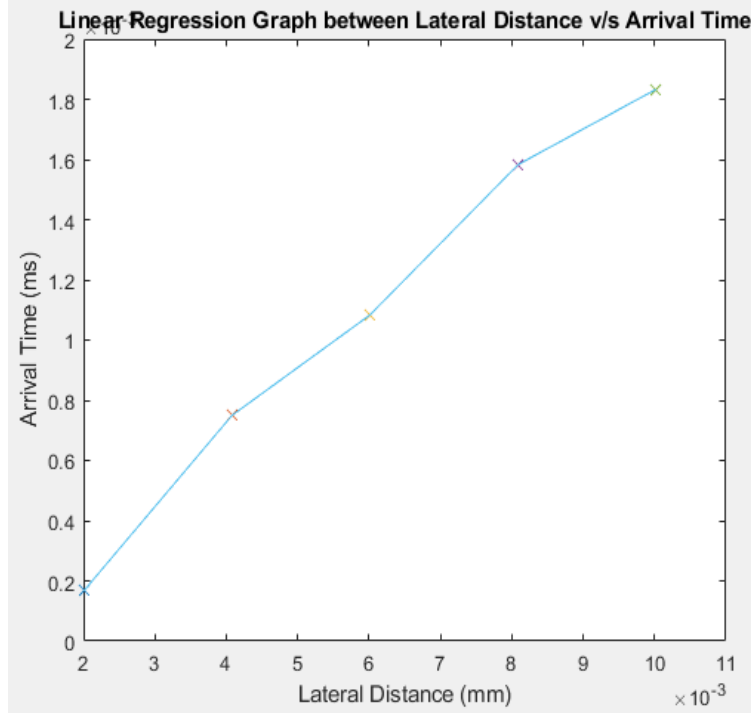
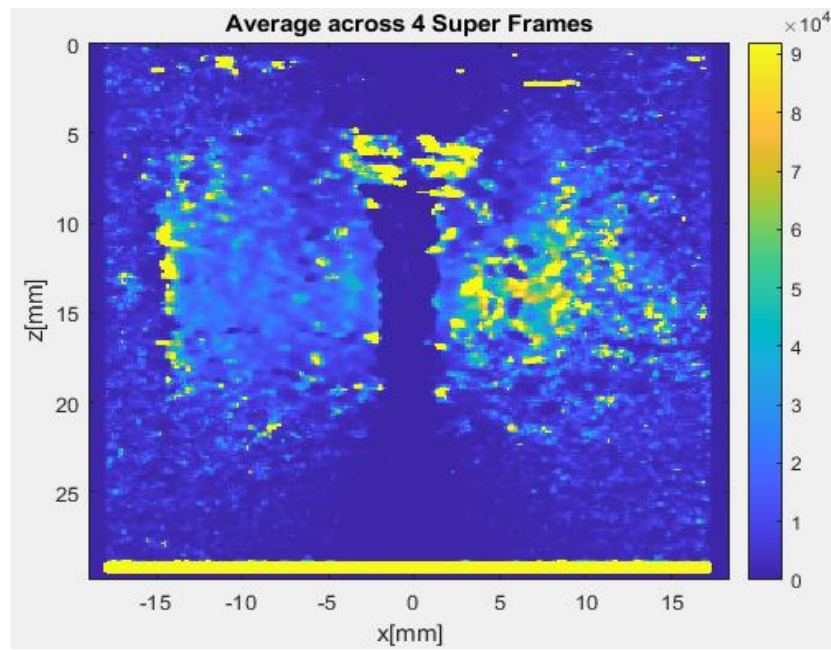


**Fig. 6.2.** Linear regression results for our 5-point example.

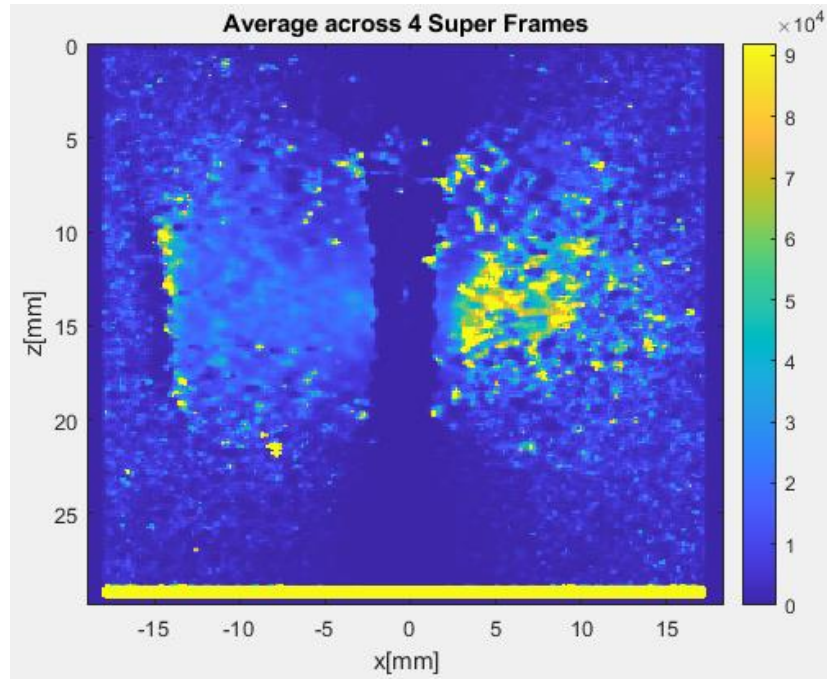
## 6.2 Elastographic Image Generation

In order to generate a shear wave elastographic image, or elastogram, we need to determine a 2D SWS profile. We accomplish the latter by using the TTP technique coupled with a laterally moving window of 2-4 mm in length [57]. That is, using an appropriately sized lateral window, we estimate the peak times, perform linear regression, square of the found SWS value to obtain the shear modulus  $\mu$  (assuming  $\rho = 1000 \text{ kg/m}^3$ ) in accordance with Eq. (40), and let the pixel value at the center of the window be equal to Young's modulus  $E = 3\mu$  [57]. Then, we move the window to its next position in the lateral direction. This process is repeated for all horizontal lines in the axial direction.

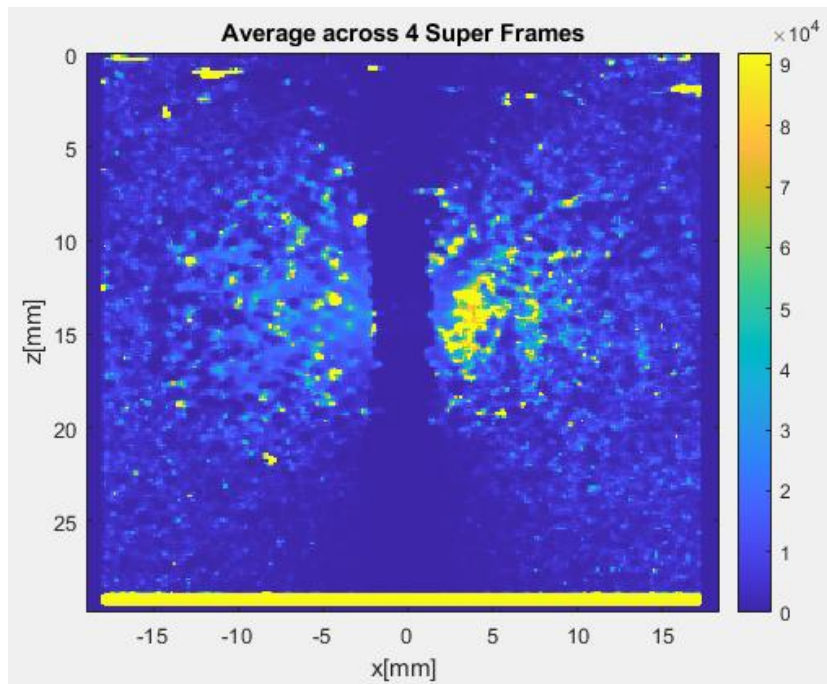
In our case, the recommended window lengths of approximately 2, 3, and 4 mm correspond to the window sizes of 13, 20, and 27 pixels, respectively. We have applied all three windows versions to our ARFI data, and then averaged the results across the super frames. The final images are shown in Figs. 6.3-6.5. Each figure contains three elastograms corresponding to the three beamforming methods under consideration: DAS, FDM, and DCT+FDM.



(a)

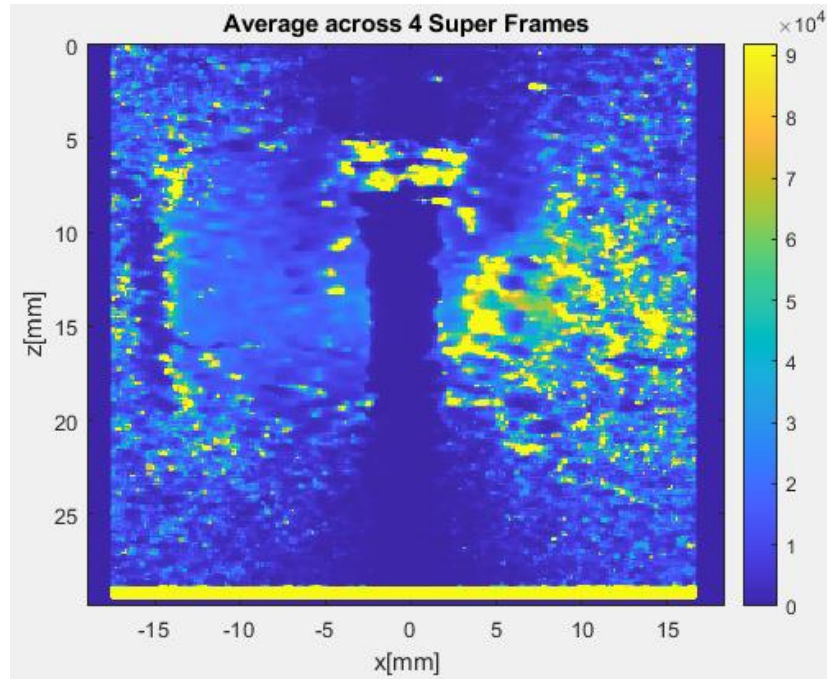


(b)

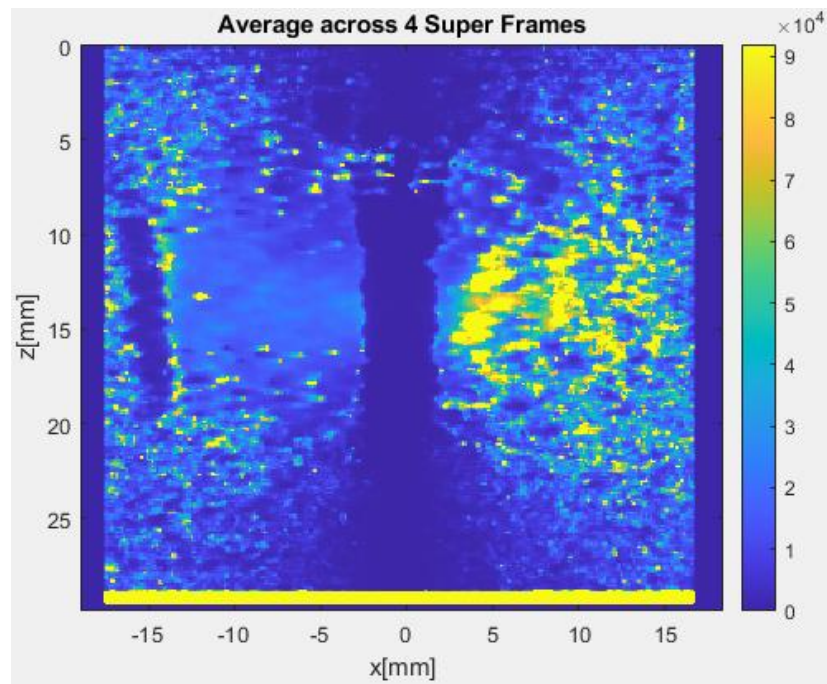


(c)

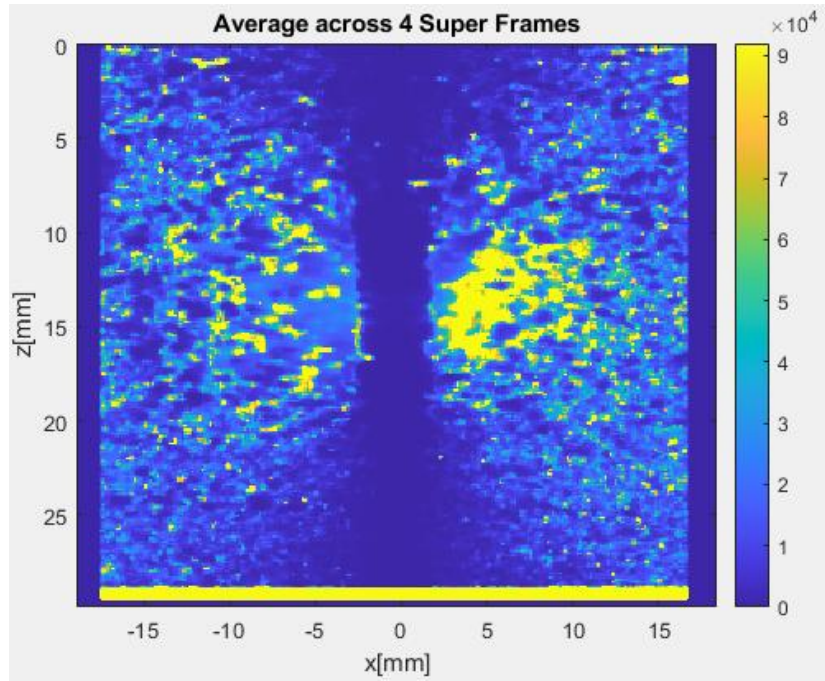
**Fig. 6.3.** Images obtained by averaging across super frames, 13-pixel window size: (a) DAS, (b) FDM and (c) DCT+FDM methods.



(a)

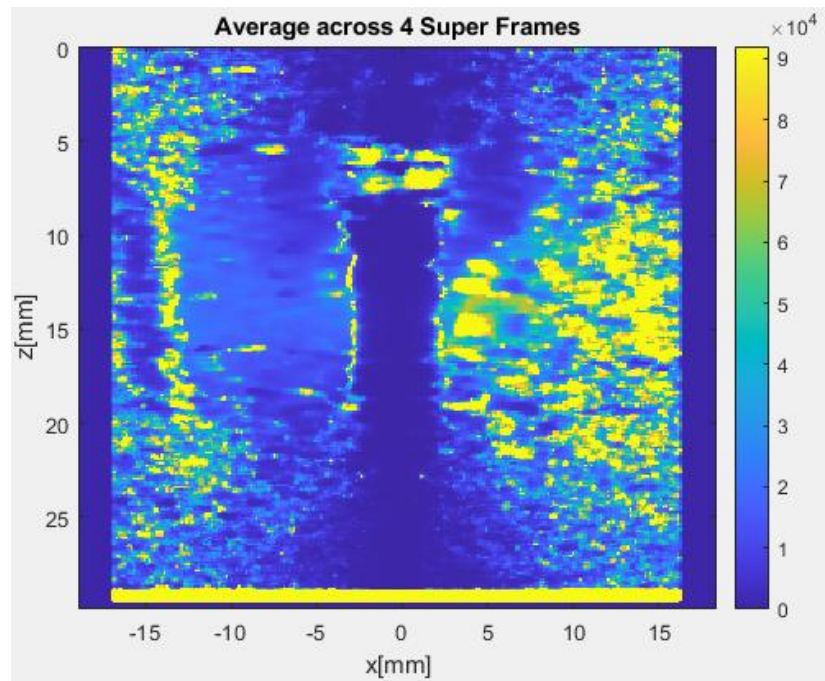


(b)

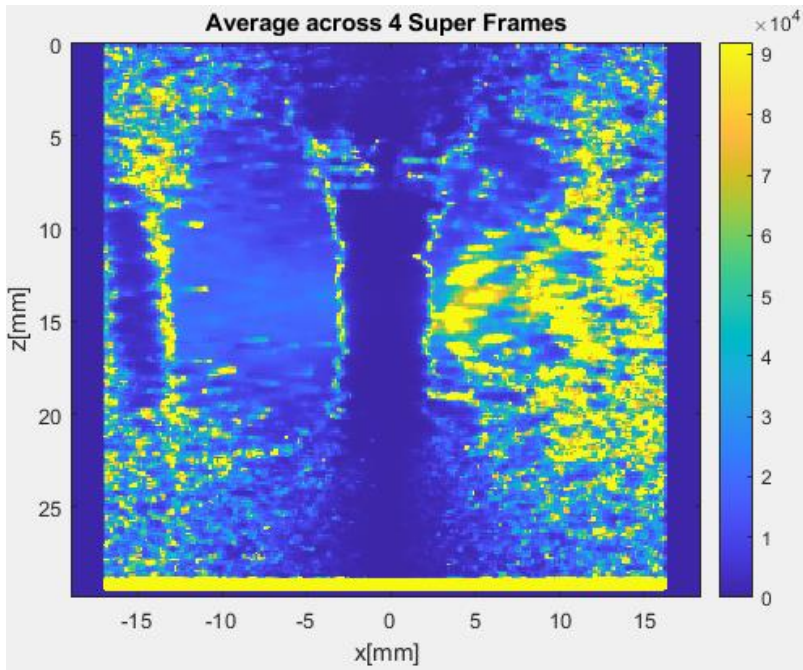


(c)

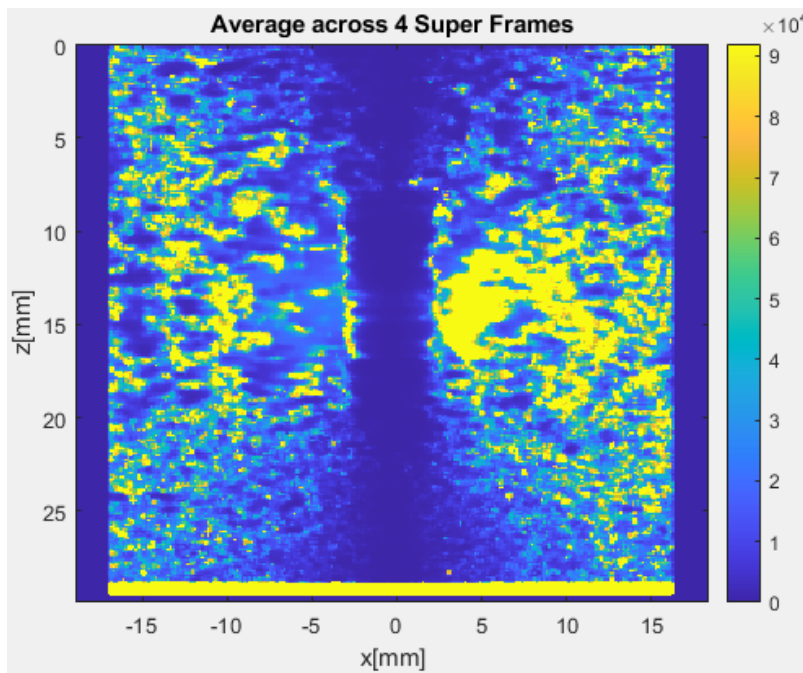
**Fig. 6.4.** Images obtained by averaging across super frames, 20-pixel window size: (a) DAS, (b) FDM and (c) DCT+FDM methods.



(a)



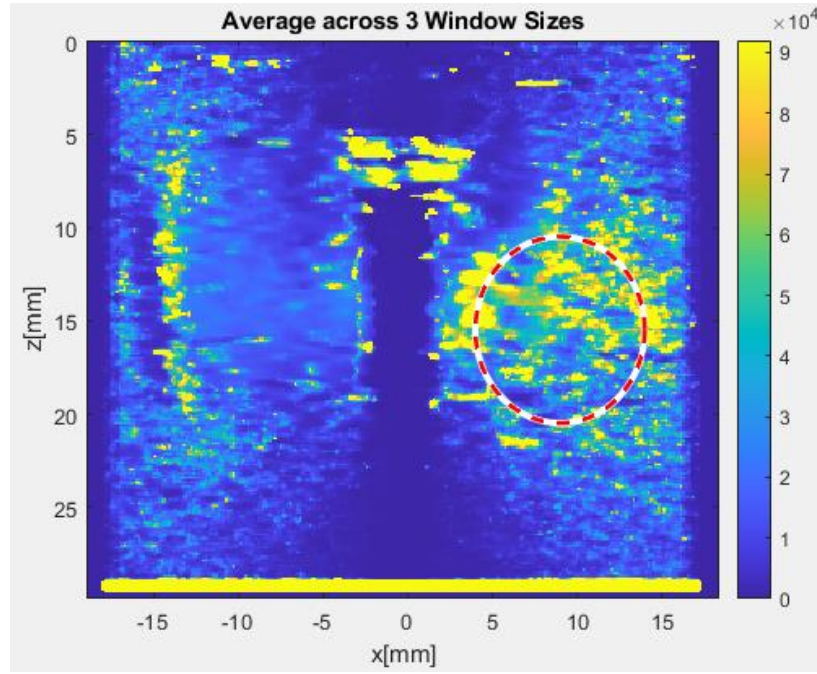
(b)



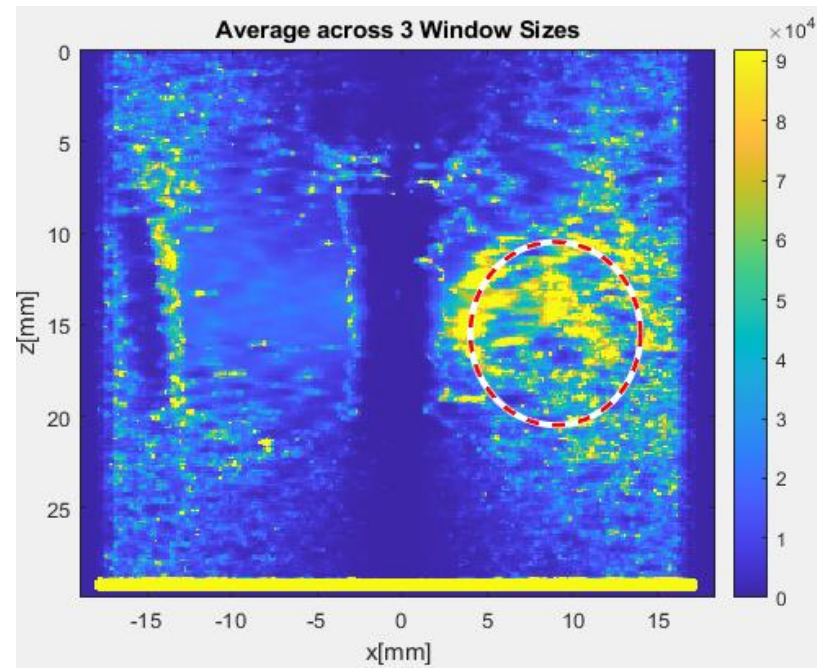
(c)

**Fig. 6.5.** Images obtained by averaging across super frames, 27-pixel window size: (a) DAS, (b) FDM and (c) DCT+FDM methods.

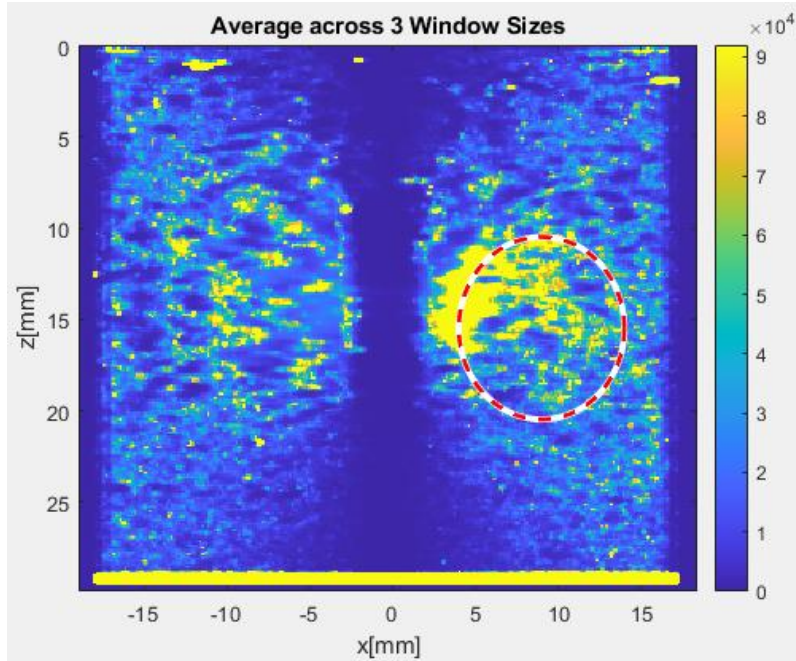
Since the images shown in Figs. 6.3-6.5 (averaged across super frames) are quite noisy, we perform additional averaging across the window sizes (i.e., 13, 20, and 27 pixels) to obtain the images shown in Fig. 6.6. The ground-truth sphere in the images is indicated by a circle.



(a)



(b)



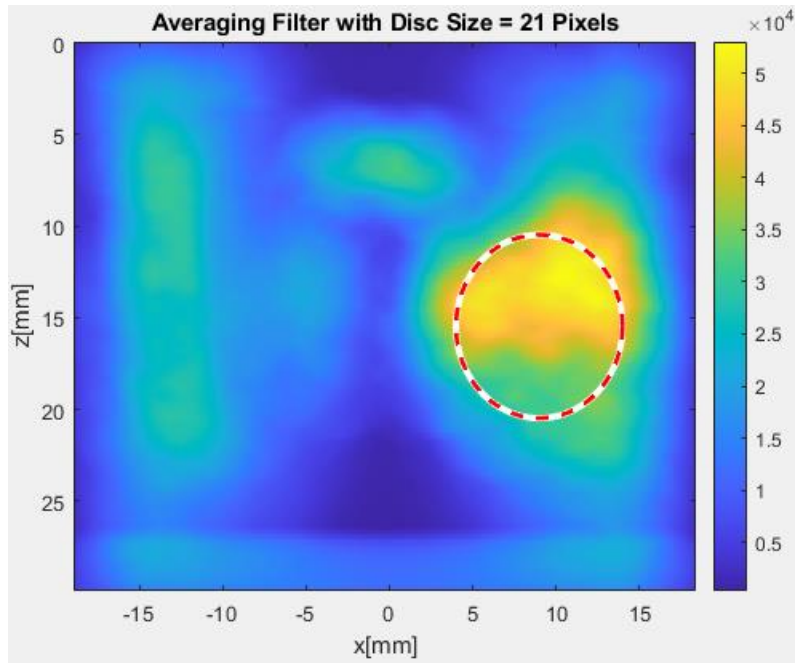
(c)

**Fig. 6.6.** Images obtained by additional averaging across window sizes: (a) DAS, (b) FDM and (c) DCT+FDM methods.

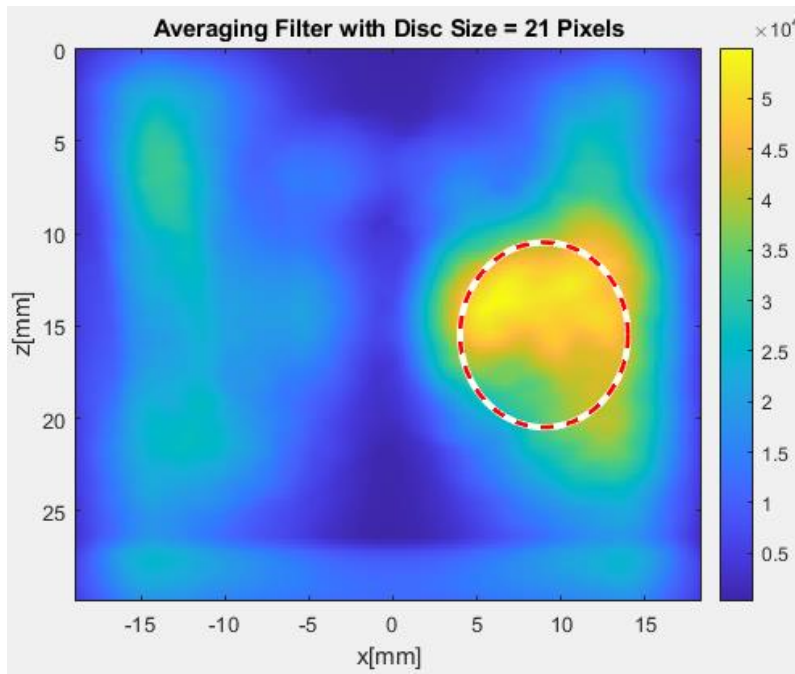
While the images in Fig. 6.6 appear slightly less noisy than those in Figs. 6.3-6.5, it is still hard to distinguish the circular shape, corresponding to the imaged 80-KPa (Type IV) 10-mm sphere embedded in the 25-KPa background. As a positive sign, we should note that the observed peak intensity of pixels inside the circular region of interest is approximately 90 KPa, which is in line with the phantom specifications ( $80 \pm 12$  KPa).

### 6.3 Post-Filtering

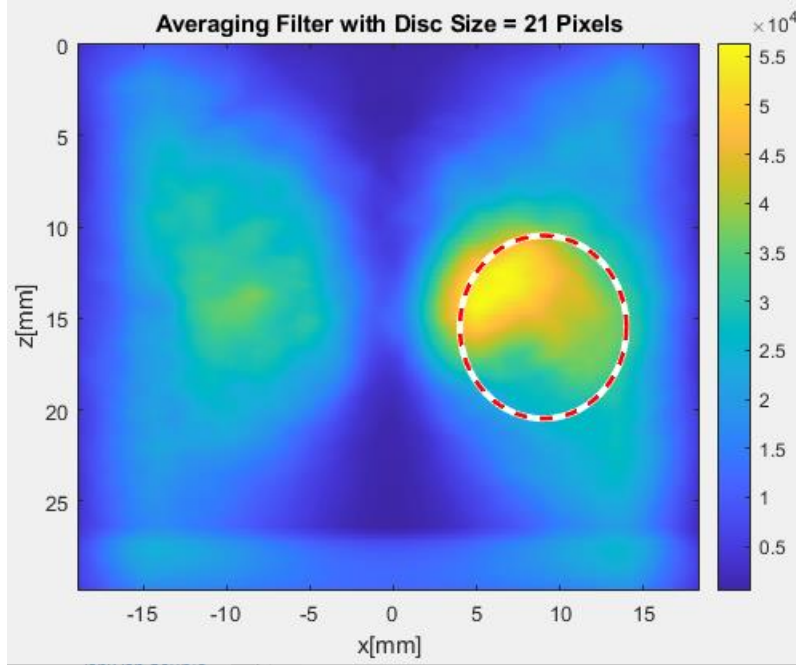
Given the noisy nature of the elastograms presented in the previous section, it is worthwhile to explore how post-filtering may improve the image quality. Figs. 6.7-6.9 show the effect of applying the averaging disc filter to the images from Fig. 6.6, using three different disc radius values: 21, 35, and 51 pixels (or approximately 6 mm, 10 mm, and 16 mm in diameter).



(a)

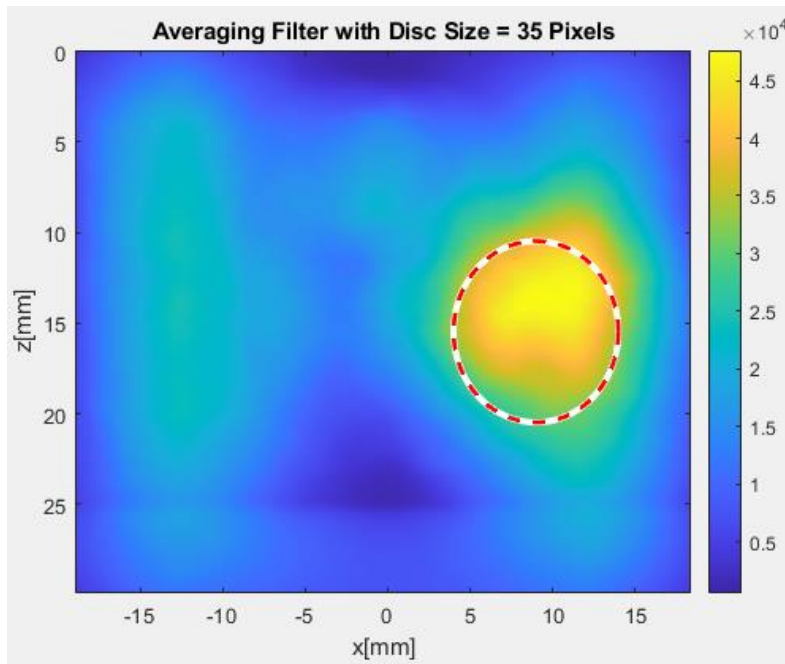


(b)

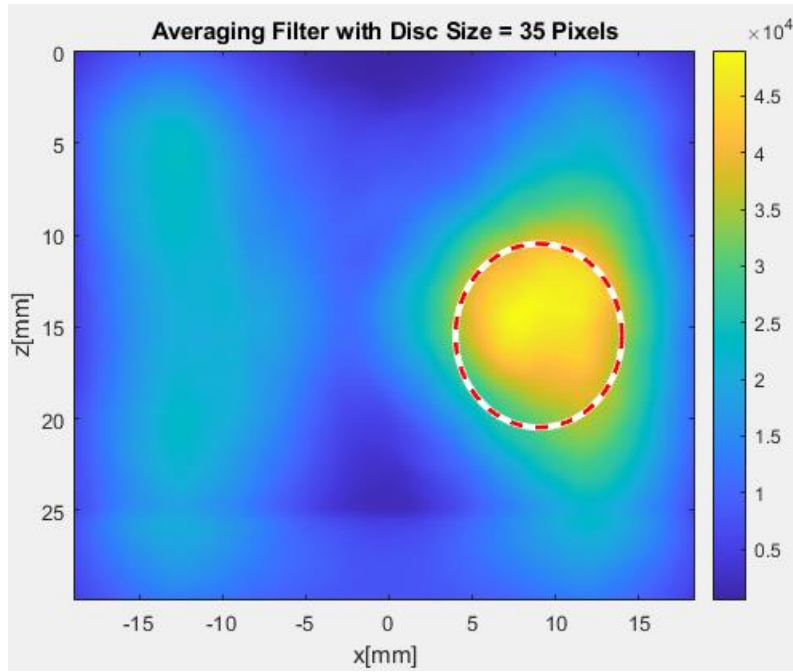


(c)

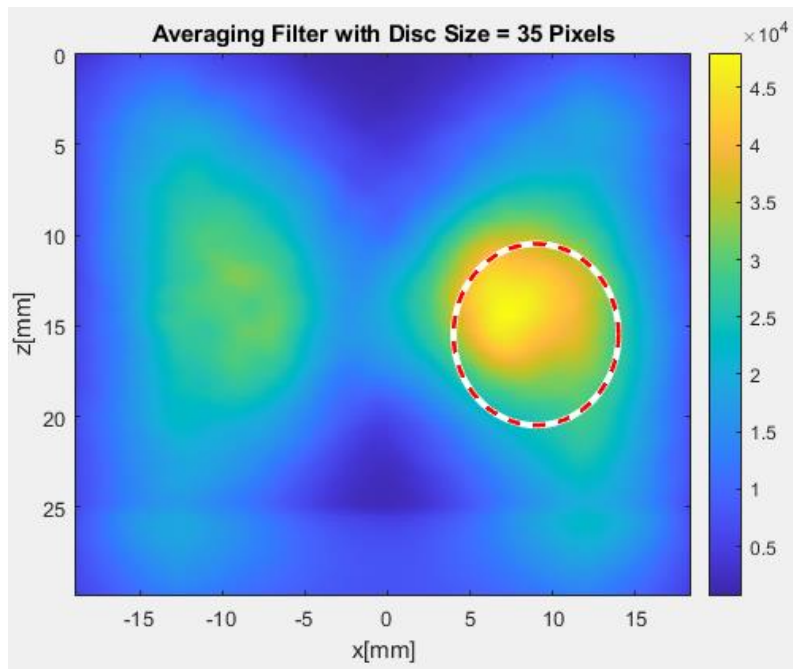
**Fig. 6.7.** Filtered elastograms after applying 21-pixel disc averaging: (a) DAS, (b) FDM and (c) DCT+FDM methods.



(a)

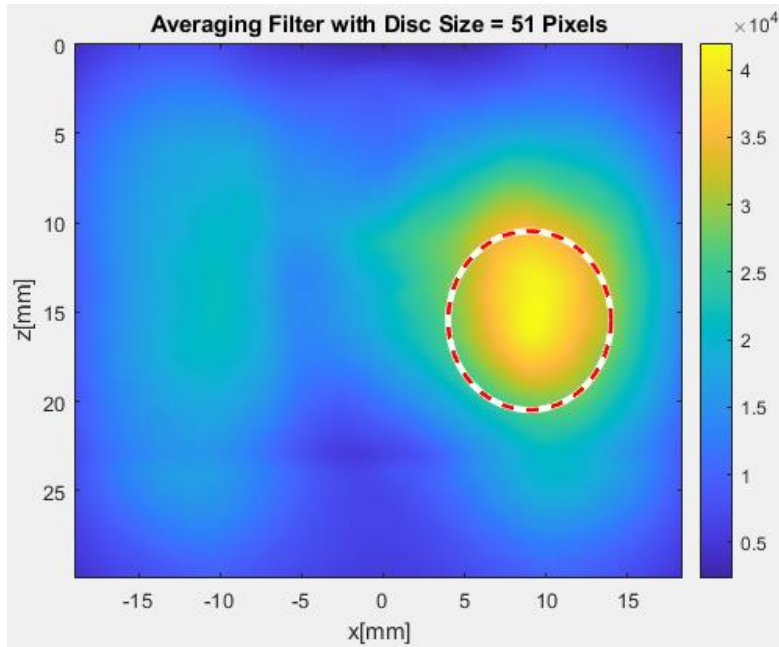


(b)

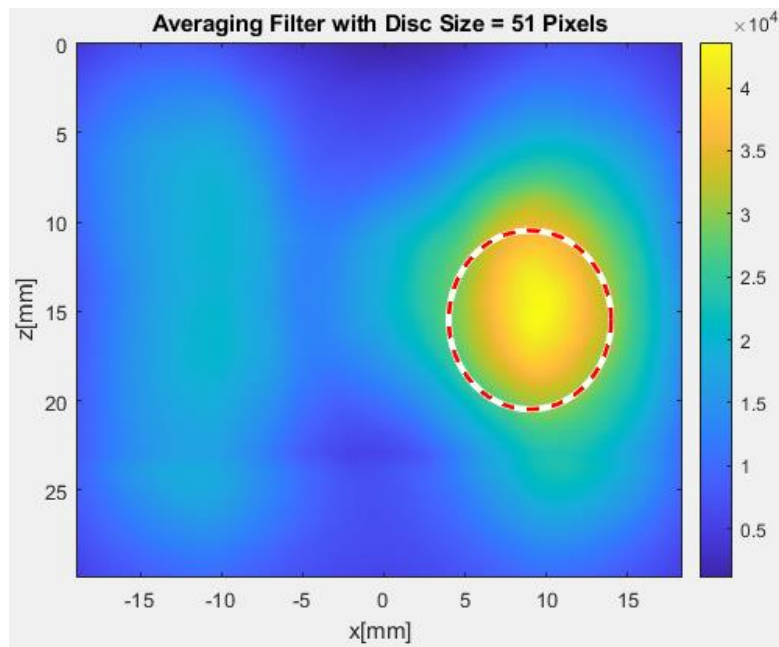


(c)

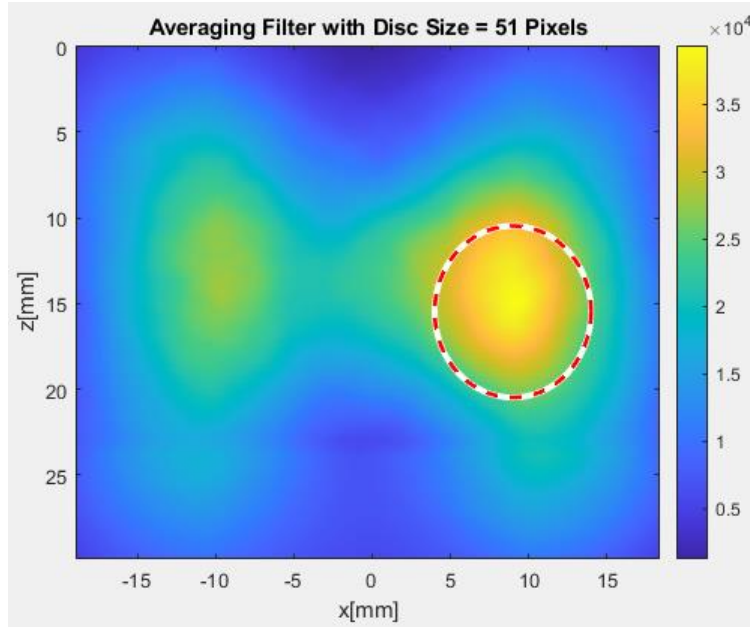
**Fig. 6.8.** Filtered elastograms after applying 35-pixel disc averaging: (a) DAS, (b) FDM and (c) DCT+FDM methods.



(a)



(b)



(c)

**Fig. 6.9.** Filtered elastograms after applying 51-pixel disc averaging: (a) DAS, (b) FDM and (c) DCT+FDM methods.

Since the imaged sphere has the diameter of 10 mm, we expect that applying the 10-mm disc filter would yield better results than its 3-mm and 16-mm competitors. Indeed, the images shown in Fig. 6.8 are arguably better than those in Figs. 6.7 and 6.9. In Fig. 6.7 only the top part of the circular region indicates higher-than-background stiffness, while in Fig. 6.9 the desired circular shape appears laterally compressed. As one can see, the FDM-based image in Fig. 6.8 (b) is very close to the DAS-based image in Fig. 6.8 (a), with  $SSIM = 0.9539$ . The similarity between the DCT+FDM-based image in Fig. 6.8 (c) and the FDM-based image in Fig. 6.8 (b) is also good, giving  $SSIM = 0.9463$ .

We should note that in Figs. 6.7-6.9 the pixel intensity is no longer accurate, peaking between approximately 40 KPa (see Fig. 6.9) and 55 KPa (see Fig. 6.7). This is due to the fact that we did not make any adjustments to the disc filter gain to maintain the 90-KPa range (see Fig. 6.6), as our focus was primarily on recovering the shape of the imaged sphere.

# Chapter 7

## Conclusion and Future Work

In this short chapter, we shall summarize our project and outline several potential directions of future research and development efforts.

### 7.1 Conclusion

This work focused on acoustic radiation force impulse (ARFI) imaging that has important applications in the area of tissue stiffness characterization. Specifically, we considered plane-wave-based tracking of the deformation response (after a pushing pulse), and investigated the imaging performance of the recently proposed Fourier-Domain Migration (FDM) method, as a faster alternative to the conventional Delay-and-Sum (DAS) beamforming method. Additionally, we explored the possibility of reducing the temporal sampling rate of an ultrasound transducer array by a factor of 2, accompanied by DCT-based interpolation to fill-in missing samples. Such rate reduction results in a 50% lower raw data acquisition cost.

Our code development was done within the MATLAB-based UltraSound ToolBox (USTB) framework. The USTB already includes reference implementations of default DAS beamforming and autocorrelation-based displacement estimation, which we have used as is. We have added our implementation of the FDM and DCT+FDM methods. The former operates on the raw data sampled at a full rate, and the latter operates on the half-rate sampled raw data that undergoes DCT interpolation before being processed by the FDM method. We have also contributed our implementation of elastographic (Young's modulus) image generation that relies on regression-based shear wave speed (SWS) estimates.

In our evaluations, we used the USTB experimental data recorded by the Verasonics research

scanner using a 128-element linear probe. The dataset consisted on 200 frames, divided into four groups, or super frames (one per push), each containing 50 plane-wave tracking frames. Plane-wave pulses were emitted at 5.208 MHz, and the returning echo signals were sampled at 20.832 MHz. The imaged target was a 10-mm 80-KPa sphere embedded in the 25-KPa background.

First, we obtained three sequences of displacement images, based on the beamformed data computed by DAS, FDM, and DCT+FDM methods (see Chapter 5). The SSIM values between DAS and FDM images ranged from 0.9010 to 0.9227, while the SSIM values between FDM and DCT+FDM images ranged from 0.8664 to 0.8918 (indicating degraded similarity due to non-ideal recovery of missing raw data samples). Then, we obtained our elastograms (shown in Fig. 6.6) by averaging Young's modulus estimates across four super frames and then across three different sliding window sizes (used for linear regression). While the resulting images showed correct Young's modulus range within the phantom specifications ( $80 \pm 12$  KPa), the desired circular shape of the target sphere was not clearly delineated. Finally, we applied averaging disc post-filtering, which noticeably improved the visual quality of the resulting elastograms. The similarity between the FDM and DCT+FDM elastograms was relatively high (SSIM = 0.9463), and the computational overhead of DCT-based interpolation was relatively small (extra 5.32%). These two facts are a promising indicator that it is possible to cut the amount of raw data samples in half and still obtain elastographic images whose quality is comparable to the full-acquisition case.

## 7.2 Future Work

One critical direction for future work is to address image noise reduction in a more aggressive and systematic fashion. For example, one can explore ideas from echocardiographic (i.e., blood flow) imaging, such as the use of decluttering filters, or apply other image denoising techniques, such as median filters, contra-harmonic mean filters, homomorphic filters, adaptive filters, etc.

Aside from designing noise reduction filters, one can also investigate how the emergent and highly effective field of Deep Learning can help with the generation of accurate elastograms. In fact, Diego Valsesia and his research group [66] have recently shown that data-driven filter

design approaches employing convolutional neural networks can outperform classical model-based filter designing techniques.

Finally, it may be worthwhile to study the effects of various subsampling and recovery schemes in the context of ARFI imaging. While many compressive sensing (CS) ideas have been successfully applied to ultrasound imaging, the computational complexity of CS recovery can be quite high. Given our experience with straightforward DCT-based interpolation (being able to adequately deal with half of the missing raw data samples), it is likely that other simple and fast recovery techniques can lead to good-quality elastographic images at a lower acquisition cost.

# Bibliography

- [1] F. Adams, *The Genuine Works of Hippocrates*. New York, NY: William Wood and Company, 1891.
- [2] E. Tohno, D. O. Cosgrove and J. P. Sloane, *Ultrasound Diagnosis of Breast Diseases*. New York, NY: Churchill Livingstone, 1994.
- [3] J. N. Wolfe, *Xeroradiography of the Breast*. Springfield, IL, Thomas, 1972.
- [4] L. Bassett, R. Gold and C. Kimme-Smith, *Hand-held and Automated Breast Ultrasound*. Thorofare, NJ: Slack, 1986.
- [5] W. L. Donegan and J. S. Spratt, *Cancer of the Breast*. Philadelphia, PA: Saunders, 2002.
- [6] J. Ophir, I. Cespedes, H. Ponnekanti, Y. Yazdi and X. Li, “*Elastography: A quantitative method for imaging the elasticity of biological tissues*”. *Ultrasonic Imaging*, vol. 13, no. 2, pp. 111–134, 1991.
- [7] J. Ophir, S. Srinivasan, R. Righetti and A. Thittai, “*Elastography: A decade of progress (2000–2010)*”. *Curr. Med. Imaging Rev.*, vol. 7, no. 4, pp. 292–312, 2011.
- [8] R. M. Lerner, S. R. Huang and K. J. Parker, “*Sonoelasticity’ images derived from ultrasound signals in mechanically vibrated tissues*”. *Ultrasound Med. Biol.*, vol. 16, no. 3, pp. 231–239, 1990.
- [9] K. J. Parker, “*The evolution of vibration sonoelastography*”. *Curr. Med. Imaging Rev.*, vol. 7, no. 4, pp. 283–291, 2011.
- [10] L. S. Wilson and D. E. Robinson, “*Ultrasonic measurement of small displacements and*

*deformations of tissue*". Ultrasonic Imaging, vol. 4, no. 1, pp. 71–82, 1982.

[11] R. J. Dickinson and C. R. Hill, "*Measurement of soft tissue motion using correlation between A-scans*". Ultrasound Med. Biol., vol. 8, no. 3, pp. 263–271, 1982.

[12] J. J. Mai and M. F. Insana, "*Strain imaging of internal deformation*". Ultrasound Med. Biol., vol. 28, no. 11–12, pp. 1475–1484, 2002.

[13] C. L. de Korte and A. F. van der Steen, "*Intravascular ultrasound elastography: An overview*". IEEE International Ultrasonics Symposium, pp. 859–865, 2002.

[14] J. D'hooge, B. Bijnens, J. Thoen, F. V. de Werf, G. R. Sutherland and P. Suetens, "*Echocardiographic strain and strain-rate imaging: A new tool to study regional myocardial function*". IEEE Transactions on Medical Imaging, vol. 21, no. 9, pp. 1022–1030, 2002.

[15] P. N. Wells and H. Liang, "*Medical ultrasound: Imaging of soft tissue strain and elasticity*". J. R. Soc. Interface, vol. 8, no. 64, pp. 1521–1549, 2011.

[16] J. F. Greenleaf, M. Fatemi and M. F. Insana, "*Selected methods for imaging elastic properties of biological tissues*". Annu. Rev. Biomed. Eng., vol. 5, no. 1, pp. 57–78, Jan. 2003.

[17] K. J. Parker, L. S. Taylor and S. Gracewski, "*A unified view of imaging the elastic properties of tissue*". J. Acoust. Soc. Am., vol. 117, no. 5, pp. 2705–2712, 2005.

[18] A. P. Sarvazyan, T. J. Hall and M. W. Urban, "*An overview of elastography—An emerging branch of medical imaging*". Curr. Med. Imaging Rev., vol. 4, no. 7, pp. 255–282, 2011.

[19] M. Albulayli and D. Rakhmatov, "*Fourier-domain depth migration for plane-wave ultrasound imaging*". IEEE Transaction on Ultrasonics, Ferroelectrics and Frequency Control, vol. 65, no. 8, pp. 1321–1333, 2018.

- [20] H. Liebgott, A. Rodriguez-Molares, F. Cervenansky, J. Jensen and O. Bernard, “*Plane-wave imaging challenge in medical ultrasound*”. IEEE International Ultrasonics Symposium, pp. 1–4, 2016.
- [21] E. Candes and J. Romberg, “*l1-MAGIC: Recovery of sparse signals via convex programming*”. Caltech, pp. 1-19, Oct 2005.
- [22] G. Montaldo, M. Tanter, J. Bercoff, N. Benech and M. Fink. “*Coherent plane-wave compounding for very high frame rate ultrasonography and transient elastography*”. IEEE Transactions on Ultrasonics, Ferroelectrics and Frequency Control, vol. 56, no. 3, pp. 489–506, 2009.
- [23] “[https://www.creatis.insalyon.fr/EvaluationPlatform/picmus/about\\_speckle\\_quality.html](https://www.creatis.insalyon.fr/EvaluationPlatform/picmus/about_speckle_quality.html)”. Plane wave Imaging Challenge in Medical UltraSound, 2018.
- [24] R. Cohen, Y. Sde-Chen, T. Chernyakova, C. Fraschini, J. Bercoff and Y. Eldar, “*Fourier domain beamforming for coherent plane-wave compounding*”. IEEE International Ultrasonics Symposium, pp. 1-4, Oct 2015.
- [25] O. Couture, M. Fink and M. Tanter, “*Ultrasound contrast plane wave imaging*”. IEEE Transactions on Ultrasonics, Ferroelectronics and Frequency Control, vol. 59, no. 12, pp. 2676-2683, 2012.
- [26] “[http://t3.trdf.co.il/show\\_invention/415](http://t3.trdf.co.il/show_invention/415)”. Frequency Domain Beamforming in Ultrasound Imaging, 2008.
- [27] “<https://patentimages.storage.googleapis.com/06/f4/9b/dd2b3776b2036c/EP2741103A1.pdf>”. Frequency-Domain Beamforming European Patent Application.
- [28] “<http://2015.icimeeting.com/e-posters/pdf/191.pdf>”. A Wireless Frequency-Domain Beamforming Based Ultrasound Imaging

- [29] S. A. Eyerly, S. J. Hsu, S. H. Agashe, G. E. Trahey, Y. Li and P. D. Wolf, “*An in vitro assessment of acoustic radiation force impulse imaging for visualizing cardiac radiofrequency ablation lesions*”. *J. Cardiovasc. Electrophysiol.*, vol. 21, no. 5, pp. 557–563, 2010.
- [30] W. M. Lai, D. Rubin and E. Krempel, *Introduction to Continuum Mechanics*. Burlington, MA: Butterworth-Heinmann, 1999.
- [31] Y. C. Fung, *Biomechanics: Mechanical Properties of Living Tissue*. 2nd ed., New York, NY: Springer-Verlag, 1993.
- [32] G. S. Kino, *Acoustic Waves: Devices, Imaging, and Analog Signal Processing*. Englewood Cliffs, NJ: Prentice-Hall, 1987.
- [33] M. L. Palmeri, A. C. Sharma, R. R. Bouchard, R. W. Nightingale and K. R. Nightingale, *A finite-element method model of soft tissue response to impulsive acoustic radiation force*. *IEEE Transactions on Ultrasonics, Ferroelectrics, and Frequency Control*, vol. 52, no. 10, pp. 1699–1712, Oct. 2005.
- [34] W. Nyborg, “*Acoustic streaming,*” in *Physical Acoustics*. vol. IIB, W. Mason, Ed. New York, NY: Academic Press, pp. 265–311, 1965.
- [35] C. Eckart, “*Vortices and streams caused by sound waves*”. *Phys. Rev.*, vol. 73, no. 1, pp. 68–76, 1948.
- [36] R. Fox and A. McDonald, *Introduction to Fluid Mechanics*. New York, NY: Wiley, 1992.
- [37] J. H. Ginsberg, “*Perturbation methods in Nonlinear Acoustics*”. M. F. Hamilton and D. T. Blackstock, Eds. San Diego, CA: Academic Press, 1997, pp. 279–308.
- [38] G. R. Torr, “*The acoustic radiation force*”. *Am. J. Phys.*, vol. 52, no. 5, pp. 402–408, 1984.

- [39] M. L. Palmeri, S. A. McAleavey, G. E. Trahey and K. R. Nightingale, “*Dynamic mechanical response of elastic spherical inclusions to impulsive acoustic radiation force excitation*”. IEEE Transactions on Ultrasonics, Ferroelectrics, and Frequency Control, vol. 53, no. 11, pp. 2065–2079, Jul. 2006.
- [40] O. Bonnefous and P. Pesque, “*Time domain formulation of pulse Doppler ultrasound and blood velocity estimation by cross correlation*”. Ultrasonic Imaging, vol. 8, no. 2, pp. 73–85, 1986.
- [41] P. Embree, “*The accurate ultrasonic measurement of the volume flow of blood by time-domain correlation*,” Ph.D. dissertation, Dept. of Electrical Engineering, University of Illinois at Urbana-Champaign, Urbana, IL, 1985.
- [42] C. Kasai, K. Namekawa, A. Koyano and R. Omoto, “*Real-time twodimensional blood flow imaging using an autocorrelation technique*”. IEEE Transactions on Sonics and Ultrasonics, vol. 32, no. 3, pp. 458–464, 1985.
- [43] T. Loupas, J. Powers and R. Gill, “*An axial velocity estimator for ultrasound blood flow imaging, based on a full evaluation of the Doppler equation by means of a two-dimensional autocorrelation approach*”. IEEE Transactions on Ultrasonics, Ferroelectrics, and Frequency Control, vol. 42, no. 4, pp. 672–688, 1995.
- [44] G. F. Pinton, J. J. Dahl and G. E. Trahey, “*Rapid tracking of small displacements with ultrasound*”. IEEE Transactions on Ultrasonics, Ferroelectrics, and Frequency Control, vol. 53, no. 6, pp. 1103–1117, 2006.
- [45] W. F. Walker and G. E. Trahey, “*A fundamental limit on delay estimation using partially correlated speckle signals*”. IEEE Transactions on Ultrasonics, Ferroelectrics, and Frequency Control, vol. 42, no. 2, pp. 301–308, 1995.
- [46] M. L. Palmeri, S. A. McAleavey, G. E. Trahey and K. R. Nightingale, “*Ultrasonic tracking*

*of acoustic radiation force-induced displacements in homogeneous media*". IEEE Transactions on Ultrasonics, Ferroelectrics, and Frequency Control, vol. 53, no. 7, pp. 1300–1313, Jul. 2006.

[47] S. A. McAleavey, K. R. Nightingale and G. E. Trahey, "*Estimates of echo correlation and measurement bias in acoustic radiation force impulse imaging*". IEEE Transactions on Ultrasonics, Ferroelectrics, and Frequency Control, vol. 50, no. 6, pp. 631–641, 2003.

[48] J. R. Doherty, J. J. Dahl and G. E. Trahey, "*A harmonic tracking method for acoustic radiation force impulse (ARFI) imaging*". IEEE International Ultrasonics Symposium, pp. 208-211, 2012.

[49] M. Albulayli and D. Rakhmatov, "*Evaluation of hybrid GSC-based and ASSB-based beamforming methods applied to ultrasound imaging*". IEEE International Conference on Acoustics, Speech and Signal Processing, pp. 5130-5134, 2012.

[50] T. Chernyakova and Y. C. Eldar. "*Fourier-domain beamforming: the path to compressed ultrasound imaging*". IEEE Transactions on Ultrasonics, Ferroelectrics, and Frequency Control, vol. 61, no. 8, pp. 1252-1267, 2014.

[51] CIRS QA Spherical Phantom Data Sheet, "<http://www.cirsinc.com/wp-content/uploads/2019/04/049-049-DS-120418.pdf>".

[52] J. R. Doherty, G. E. Trahey, K. R. Nightingale and M. L. Palmeri. "*Acoustic radiation force elasticity imaging in diagnostic ultrasound*". IEEE Transaction on Ultrasonics, Ferroelectrics, and Frequency Control, vol. 60, no. 4, pp. 685-701, 2013

[53] R. Ahmed, S. A. Gerber, S. A. McAleavey, G. Schifitto and M. M. Doyley, "*Plane wave imaging improves single track location shear wave elasticity imaging*". IEEE Transaction on Ultrasonics, Ferroelectrics and Frequency Control, vol. 65, issue. 8, Aug. 2018.

- [54] T. Sugimoto, S. Ueha and K. Itoh, “*Tissue hardness measurement using the radiation force of focused ultrasound*”. IEEE Transactions on Ultrasonics, Ferroelectrics, and Frequency Control, pp. 1377–1380, 1990.
- [55] J. McLaughlin and D. Renzi. “*Shear wave speed recovery in transient elastography and supersonic imaging using propagating fronts*”. Inverse Problems, 22(2):681–706, 2006.
- [56] M. L. Palmeri, M. H. Wang, J. J. Dahl, K. D. Frinkley and K. R. Nightingale, “*Quantifying hepatic shear modulus in vivo using acoustic radiation force*”. Ultrasound in Medicine and Biology, 34(4):546–558, 2008.
- [57] M. Tanter, J. Bercoff, A. Athanasiou, T. Deffieux, J. L. Gennisson, G. Montaldo, M. Muller, A. Tardivon and M. Fink, “*Quantitative assessment of breast lesion viscoelasticity: initial clinical results using supersonic shear imaging*”. Ultrasound in Medicine and Biology, 34(9):1373–1386, 2008.
- [58] A. C. Schmitz et al. “*Image-guided focused ultrasound ablation of breast cancer: current status, challenges, and future directions*”. Eur Radiol 18, pp. 1431–1441, 2008.
- [59] S. Thüroff, C. Chaussy, G. Vallancien, W. Wieland, H. J. Kiel, A. le Duc, F. Desgrandchamps, J. de la Rosette and A. Gelet, “*High-intensity focused ultrasound and localized prostate cancer: efficacy results from the European multicentric study*”. Journal of Endourology, pp. 673-677, Oct 2003.
- [60] H. L. V. Trees, *Optimum Array Processing*. New York, NY: Wiley, 2002
- [61] A. Rodriguez-Molares, O. M. H. Rindal, O. Bernard, A. Nair, M. A. L. Bell, H. Liebgott, A. Austeng and L. Løvstakken, “*The UltraSound ToolBox*”. IEEE International Ultrasonics Symposium, pp. 1-4, 2017.

- [62] T. K. Borstad, “*Comparison of three ultrasound velocity estimators for strain imaging of the brain*”. NTNU, 2010.
- [63] M. Polichetti, F. Varray, J.-C. Bera, C. Cachard and B. Nicolas, “*A nonlinear beamformer based on  $p$ -th root compression—application to plane wave ultrasound imaging*”. Applied Sciences, pp. 1-15, Apr. 2018.
- [64] Z. Wang, A. C. Bovik, H. R. Sheikh and E. P. Simoncelli, “*Image quality assessment: From error visibility to structural similarity*”, IEEE Transactions on Image Processing, vol. 13, no. 4, pp. 600-612, Apr. 2004.
- [65] Dr. Wu-Sheng Lu, Department of Electrical and Computer Engineering, University of Victoria, Victoria, Canada, “*ECE-503 Course Notes: Optimization for Machine Learning*”, 2019.
- [66] D. Valsesia, G. Fracastoro and E. Magli, “*Image Denoising with Graph-Convolutional Neural Networks*”. IEEE International Conference on Image Processing, pp. 1-9, 2019.
- [67] R. C. Gonzalez and R. E. Woods, *Digital Image Processing*, 3rd ed., Englewood Cliffs, NJ: Prentice-Hall, 2008.
- [68] Dr. Wu-Sheng Lu, Department of Electrical and Computer Engineering, University of Victoria, Victoria, Canada, “*ECE-534 Course Notes: Application of Digital Signal Processing Techniques*”, 2018.
- [69] Julius O. Smith III, *Mathematics of the Discrete Fourier Transform (DFT) with Audio Applications*. Center for Computer Research in Music and Acoustics (CCRMA), Department of Music, Stanford University, Stanford, California, 1977.
- [70] C.-W. Kok and W.-S Tam, *Digital Image Interpolation in MATLAB*. New York, NY: Wiley, 2018.
- [71] M. Albulayli, “*Migration-Based Image Reconstruction Methods for Plane-Wave Ultrasound Imaging*”. PhD thesis, University of Victoria, Victoria, Canada, 2018.